"Eddy" saturation of the Antarctic Circumpolar Current by standing waves

Andrew L. Stewart,[a] Nicole K. Neumann,[b] and Aviv Solodoch,[a]

[a] *Department of Atmospheric and Oceanic Sciences, University of California, Los Angeles, Los Angeles, California, USA*
[b] *Columbia Climate School, Lamont-Doherty Earth Observatory, Palisades, New York, USA*

ABSTRACT: It is now well established that changes in the zonal wind stress over the ACC do not lead to changes in its baroclinicity nor baroclinic transport, a phenomenon referred to as "eddy saturation". Previous studies provide contrasting dynamical mechanisms for this phenomenon: on one extreme, changes in the winds lead to changes the efficiency with which transient eddies transfer momentum to the sea floor; on the other, structural adjustments of the ACC's standing meanders increase the efficiency of momentum transfer. In this study the authors investigate the relative importance of these mechanisms using an idealized, isopycnal channel model of the ACC. Via separate diagnoses of the model's time-mean flow and eddy diffusivity, the authors decompose the model's response to changes in wind stress into contributions from transient eddies and the mean flow. A key result is that holding the transient eddy diffusivity constant while varying the mean flow very closely compensates changes in the wind stress, whereas holding the mean flow constant and varying the eddy diffusivity does not. This implies that "eddy saturation" primarily occurs due to adjustments in the ACC's standing waves/meanders, rather than due to adjustments of transient eddy behavior. The authors derive a quasi-geostrophic theory for ACC transport saturation by standing waves, in which the transient eddy diffusivity is held fixed, and thus provides dynamical insights into standing wave adjustment to wind changes. These findings imply that representing eddy saturation in global models requires adequate resolution of the ACC's standing meanders, with wind-responsive parameterizations of the transient eddies being of secondary importance.

1. Introduction

The response of the Southern Ocean to changes in the atmospheric state and circulation has been the subject of extensive scientific study in recent decades (see *e.g.* Mayewski et al. 2009; Rintoul 2018). This scientific scrutiny is motivated by the central role of the Southern Ocean, and particularly the Antarctic Circumpolar Current (ACC), in connecting the major ocean basins (Nowlin Jr and Klinck 1986; Olbers et al. 2004) and closing the deep cells of the global overturning circulation (Marshall and Speer 2012; Talley 2013). Particular emphasis has been placed on the strengthening and southward-shifting of the southern hemisphere westerlies that occurs with increased atmospheric CO_2 concentrations, both as a consequence of anthropogenic influence (Hazel and Stewart 2019; Thompson and Solomon 2002) and naturally over paleoclimatic time scales (Toggweiler et al. 2006; Toggweiler 2009).

It is now a well-established result, both based on observations (Böning et al. 2008) and model simulations (Meredith and Hogg 2006; Hogg and Blundell 2006; Meredith et al. 2012), that the baroclinic transport of the ACC is approximately insensitive to changes in the westerly winds. This phenomenon, referred to as "eddy saturation" (Straub 1993; Hogg et al. 2008), apparently contradicts the historical conception of the ACC as a primarily wind-driven current (Munk and Palmén 1951; Nowlin Jr and Klinck 1986). Indeed, idealized model experiments have shown that the ACC transport may remain insensitive to winds even at the limit of zero wind stress (Munday et al. 2013), provided that mesoscale eddies are sufficiently well resolved and that the meridional overturning circulation is sufficiently weak (Youngs et al. 2019).

Figure 1 illustrates schematically the mechanism via which eddy saturation occurs. This mechanism is most clearly isolated in a quasi-latitudinal coordinate system that follows mean streamlines of the ACC, which emphasizes the role of mesoscale eddies, rather than time-mean flows (Abernathey and Cessi 2014). In an equilibrium state, momentum is transferred from the winds into the upper ocean, and is then transferred down to the deep ocean (and ultimately the sea floor) via eddy interfacial form stress (IFS) (Marshall and Radko 2003; Abernathey and Cessi 2014). The eddy IFS results from baroclinic instabilities, which draw energy from the baroclinicity of the ACC (Treguier and McWilliams 1990; Youngs et al. 2017). "Eddy saturation" refers to the response of this system to a change in surface wind stress: increasing the surface wind stress leads to a commensurate increase in the eddy IFS, while the baroclinicity of the ACC remains unchanged. We note that this characterization of "eddy saturation" in terms of eddy IFS is equivalent (under quasi-geostrophic scaling) to previous characterizations based on quasi-meridional Ekman vs. eddy volume transports (*e.g.* Thompson and Naveira Garabato 2014; Youngs et al. 2019).

Previous studies of the "eddy saturation" phenomenon have proposed diverging mechanistic explanations. On one extreme, "eddy saturation" has been posited to result from changes in the efficiency of the transient eddy IFS (or, equivalently, the horizontal eddy buoyancy flux), char-

Corresponding author: Andrew L. Stewart, astewart@atmos.ucla.edu

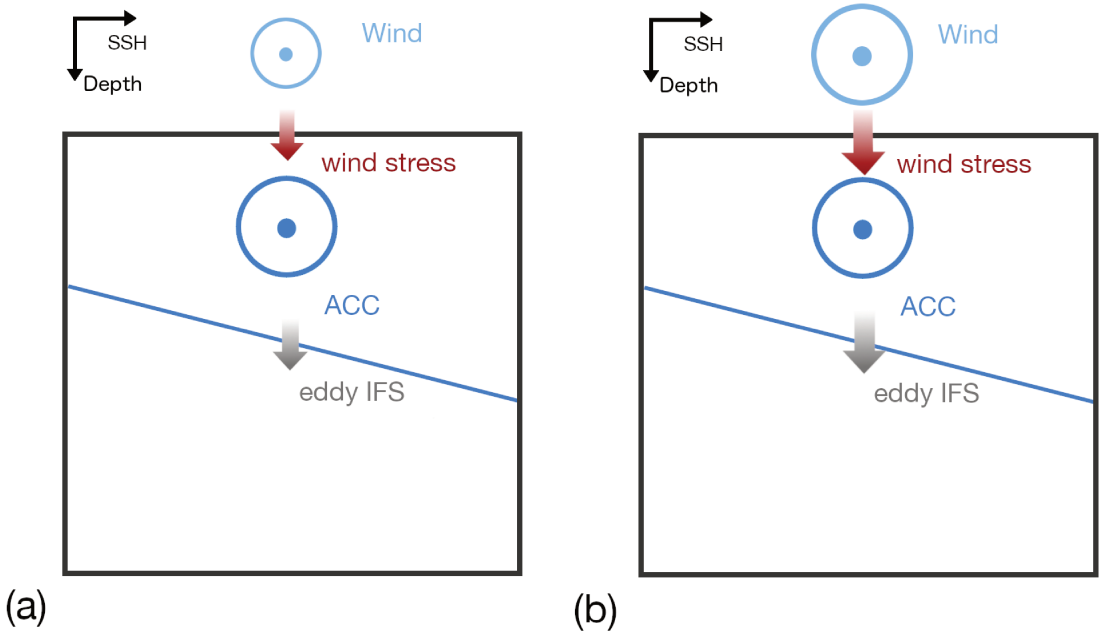

FIG. 1. Schematic of the eddy saturation phenomenon, presented in a coordinate system that follows the time-mean geostrophic streamlines of the ACC, which for the upper ocean is the sea surface height (SSH). In each panel the tilted blue line schematically indicates an isopycnal surface, and the blue arrow (directed out of the page) indicates the near-surface flow of the ACC. (a) Momentum input by the wind (light blue arrow, out of the page) to the upper ocean is transferred downward by eddy interfacial form stress (IFS) to the deep ocean, where it is ultimately removed by topographic form stress and bottom friction. (b) Increases in the zonal surface wind stress lead to commensurate increases in the eddy IFS, with approximately no change in the baroclinicity of the ACC. Note that the geostrophic streamline-following coordinate system ensures there is no mean component of the IFS (see Section 2b and Abernathey and Cessi 2014).

acterized by the Gent-McWilliams diffusivity, κ (Gent and McWilliams 1990; Gent et al. 1995). For example, the residual-mean theory of Marshall and Radko (2003, 2006) requires that κ scale linearly with the wind stress in order to preserve the baroclinicity of the ACC. Meredith et al. (2012) rationalized this linear scaling based on the mixing suppression theory of Ferrari and Nikurashin (2010). More recently, Marshall et al. (2017) and Mak et al. (2018) have developed a theory for changes in κ based on the eddy energy budget, constraining the eddy interfacial form stress following the geometric interpretation of Marshall et al. (2012) and Maddison and Marshall (2013). This theory explicitly predicts approximate independence of the ACC transport on wind stress, but relatively strong dependence of the ACC transport on friction at the sea floor (Marshall et al. 2017; Mak et al. 2018, 2022).

On the other extreme, "eddy saturation" has been posited to result from adjustment of the ACC's time-mean standing meanders, *i.e.* standing Rossby waves (Marshall 2016; Bai et al. 2021). Thompson and Naveira Garabato (2014) noted that two-dimensional residual-mean theories of the ACC omit the zonally-localized dynamics of the ACC's standing meanders, where eddy activity is concentrated (Abernathey and Cessi 2014; Meredith 2016; Rintoul 2018). Based on analysis of a high-resolution global ocean model, Thompson and Naveira Garabato (2014) proposed that the ACC could adjust to changes in zonal wind stress via "flexing" of its standing meanders, *i.e.* changes in the meander shape and amplitude that serve to increase or decrease the efficiency of downward momentum transfer by mean IFS. Nadeau and Ferrari (2015) used channel model simulations to show that eddy saturation does not occur in the absence of bathymetric obstacles and standing meanders, and proposed that formation of closed gyres abutting the flow of the ACC plays a key role in balancing increases in zonal wind stress. Constantinou and Hogg (2019) showed that "eddy saturation" occurs even in barotropic channel model simulations, in which there can be no baroclinic instability, and thus concluded that barotropic flow-topographic interactions alone are sufficient to produce a saturation response.

Thus there remains an outstanding question as to what extent "eddy saturation" occurs as a result of changes in the efficiency of transient eddy transfer, versus rearrangement of the ACC's standing meanders. In this study we address this question by using an idealized isopycnal channel

model to quantify the relative importance of transient eddy versus standing wave adjustment in "eddy saturation". In Section 2 we describe our numerical configuration, pose a decomposition of the eddy saturation response via the momentum balance along time-mean geostrophic streamlines, and present a method of diagnosing the transient eddy diffusivity. In Section 3 we examine the saturation response simulated across a suite of model experiments, and apply our decomposition to distinguish the roles of transient eddy versus standing wave adjustment. Motivated by these findings, in Section 4 we pose a quasi-geostrophic standing wave theory of eddy saturation, and use it to draw insights into the dynamics of standing wave adjustment to wind changes. Finally, in Section 5 we discuss our findings and conclude.

2. Numerical modeling approach and diagnostics

a. Model configuration

We designed our model configuration to minimize physical complexity while capturing the "eddy saturation" phenomenon, drawing inspiration from many previous studies of ACC dynamics (Ward and Hogg 2011; Nadeau and Ferrari 2015; Howard et al. 2015; Constantinou and Hogg 2019; Youngs et al. 2019). Specifically, we simulate the flow in a zonally re-entrant walled channel of zonal length $L_x = 3200\,\mathrm{km}$, meridional width $L_y = 1600\,\mathrm{km}$, and depth $H = 4000\,\mathrm{m}$. The channel is posed on a mid-latitude beta-plane with Coriolis parameter $f = f_0 + \beta(y - L_y/2)$, where $f_0 = -1\times10^{-4}\,\mathrm{s}^{-1}$ is the reference Coriolis parameter and $\beta = 1.5\times10^{-11}\,\mathrm{m}^{-1}\,\mathrm{s}^{-1}$ is the Coriolis parameter gradient. To obstruct the zonal flow through the channel, we impose a single Gaussian bump in the sea floor ($z = \eta_\mathrm{b}(x)$) at $x = X_\mathrm{b} = 1000\,\mathrm{km}$ of height $H_\mathrm{b} = 1000\,\mathrm{m}$ and width $W_b = 150\,\mathrm{km}$,

$$\eta_\mathrm{b} = -H + H_\mathrm{b}\exp\left[-\left(\frac{x - X_\mathrm{b}}{W_\mathrm{b}}\right)^2\right]. \tag{1}$$

This geometry, shown in Figure 2, crudely represents the presence of bathymetric obstacles that generate standing meanders in the ACC (*e.g.* Thompson and Naveira Garabato 2014; Nadeau and Ferrari 2015; Youngs et al. 2019).

The density stratification is represented by two layers, each of constant density, as this is the minimum required to allow the development of baroclinic instability (Vallis 2006). The isopycnal velocities and layer thicknesses evolve according to conservation of momentum, which we write for convenience as

$$\frac{\partial}{\partial t}(h_k\boldsymbol{u}_k) + \nabla\cdot(h_k\boldsymbol{u}_k\boldsymbol{u}_k) + (-1)^k\omega\boldsymbol{u}^\star + f\hat{\boldsymbol{z}}\times h\boldsymbol{u} + h_k\nabla M_k = \delta_{1,k}\frac{\boldsymbol{\tau}_\mathrm{w}}{\rho_0} - \delta_{2,k}\frac{\boldsymbol{\tau}_\mathrm{b}}{\rho_0} + \nabla\cdot\boldsymbol{\sigma}_k, \tag{2}$$

and conservation of volume,

$$\frac{\partial h_k}{\partial t} + \nabla\cdot(h_k\boldsymbol{u}_k) + (-1)^k\omega = 0. \tag{3}$$

We denote the isopycnal velocity in each layer as $\boldsymbol{u}_k$ and the corresponding layer thickness as h_k, where $k = 1$ corresponds to the upper layer and $k = 2$ to the lower layer. We make the rigid-lid approximation to exclude fast surface gravity waves, so the Montgomery potential M_k is defined as

$$M_k = \pi + \delta_{2,k}\,g'\eta. \tag{4}$$

Here π is the surface pressure (normalized by the reference density), $\eta = -h_1$ is the elevation of the interface between the layers, $g' = g\Delta\rho/\rho_0 = 1\times10^{-2}\,\mathrm{m\,s}^{-2}$ is the reduced gravity, $\Delta\rho$ denotes the positive density difference between the layers, g is the gravitational constant, $\rho_0 = 1000\,\mathrm{kg\,m}^{-3}$ is a reference density, and δ denotes the Kronecker delta.

The flow in the upper layer is forced by a zonal wind stress $\tau_\mathrm{w}(y)\hat{\boldsymbol{x}}$ whose latitudinal structure (see Figure 2(a)) is given by

$$\tau_\mathrm{w}(y) = \tau_\mathrm{w}^\mathrm{max}\sin^2\left(\frac{\pi y}{L_y}\right), \tag{5}$$

where $\hat{\boldsymbol{x}}$ denotes a unit vector in the x-direction. The flow in the lower layer is retarded by frictional stress $\boldsymbol{\tau}_\mathrm{b}$ at the sea floor. For all experiments described in the main text, we adopt a quadratic formulation of this frictional stress,

$$\boldsymbol{\tau}_\mathrm{b} = \rho_0 C_\mathrm{d}|\boldsymbol{u}_2|\boldsymbol{u}_2, \tag{6}$$

where C_d is the drag coefficient. We perform an analogous set of experiments, results of which are presented in Appendix B, using a linear formulation of the frictional stress,

$$\boldsymbol{\tau}_\mathrm{b} = \rho_0 r_\mathrm{b}\boldsymbol{u}_2, \tag{7}$$

where r_b is the friction velocity. Over the northernmost 100 km of the model domain we impose a diapycnal velocity

$$\omega = \frac{\eta - \eta^0}{T_\mathrm{relax}}, \tag{8}$$

that serves to relax the layer interface toward a reference elevation $\eta^0 = -1750\,\mathrm{m}$. The relaxation rate T_relax^{-1} varies linearly from $1\,\mathrm{week}^{-1}$ at the northern wall to zero at the edge of the restoring region. This relaxation is not strictly necessary in our model configuration because the flow can be configured to be perfectly adiabatic, but it serves to produce a consistent stratification at the northern edge of the domain across our experiments, without constraining the isopycnal slope across the channel. The diapycnal velocity also enters (2) in order to conserve momentum, multiplying an effective isopycnal velocity $\boldsymbol{u}^\star$ that is assigned based on the layer that is "upwind" relative to the diapycnal velocity

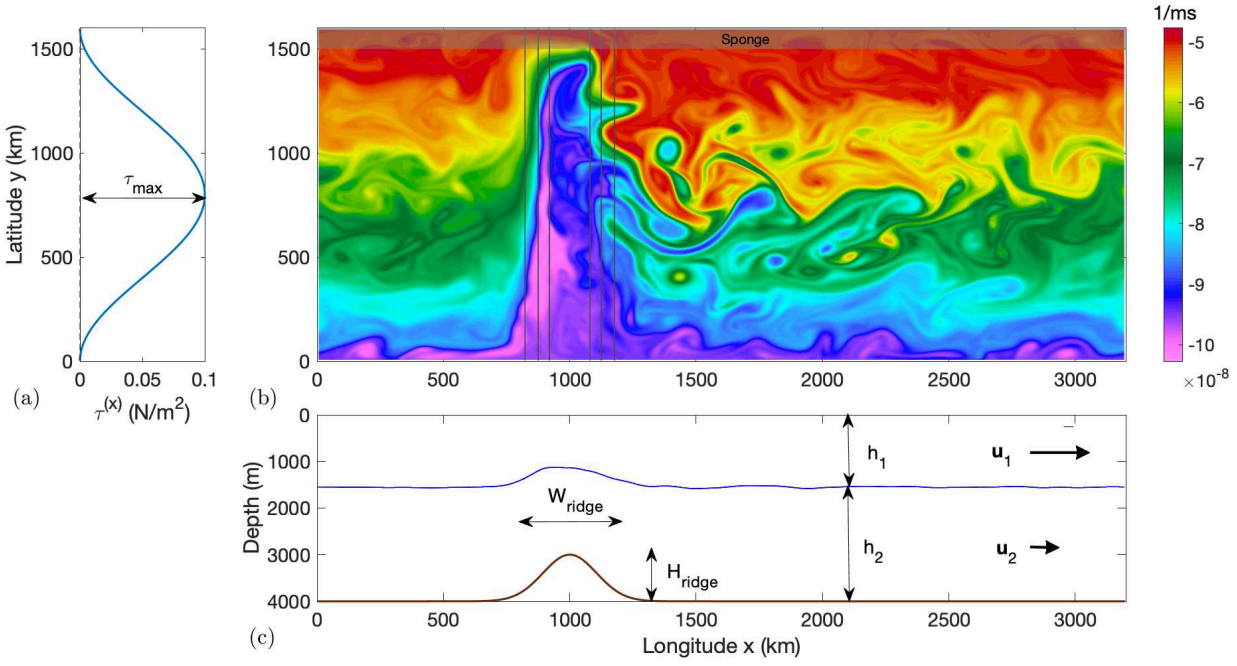

FIG. 2. Schematic of our model configuration. (a) Latitudinal profile of zonal wind stress applied to the upper isopycnal layer. (b) Snapshot of potential vorticity in the upper isopycnal layer of our reference simulation. Shading indicates the location of the sponge/restoring region at the northern boundary, while dark gray contours indicate the 3750 m, 3500 m and 3250 m isobaths. (c) Zonal variation of the topographic elevation (brown) and the meridionally-averaged isopycnal layer interface (blue) corresponding to the simulation snapshot shown in panel (b).

(LeVeque 2002),

$$\boldsymbol{u}^\star = \begin{cases} \boldsymbol{u}_1, & \omega < 0, \\ \boldsymbol{u}_2, & \omega > 0. \end{cases} \tag{9}$$

Finally we dissipate grid-scale energy and enstrophy via a biharmonic viscous stress tensor, $\nabla \cdot \boldsymbol{\sigma}_k$, using a Smagorinsky prescription of the viscosity with dimensionless coefficient $A_{\mathrm{Smag}} = 4$ (Griffies and Hallberg 2000).

We solve (2)–(4) via forward numerical integration using the AWSIM model (Stewart and Dellar 2016). We adopt the same spatio-temporal numerical schemes as those discussed by Stewart et al. (2021). We discretize the model equations on a uniform horizontal grid of $N_x \times N_y = 512 \times 256$ points, corresponding to a grid spacing of approximately 6 km. The horizontal grid spacing is chosen to be much smaller than the baroclinic deformation radius, in order to ensure adequate resolution of mesoscale eddies (Hallberg 2013). For our chosen model parameters the baroclinic deformation radius is approximately 30 km, which is comparable to the first Rossby radius of deformation along the northern flank of the ACC (Chelton et al. 1998).

Motivated by the previous finding that bottom friction plays an important role in setting the ACC transport, we conduct a suite of experiments in which we co-vary the wind stress ($\tau_{\mathrm{w}}^{\max} = \{0.01, 0.013, 0.017, 0.022, 0.03, 0.039, 0.05, 0.07, 0.1, 0.13, 0.17, 0.22, 0.3, 0.39, 0.5\}\,\mathrm{N\,m^{-2}}$) with either the quadratic drag coefficient ($C_{\mathrm{d}} = \{.5, 1, 1.5, 2, 2.5, 3, 3.5, 4\} \times 10^{-3}$) or the linear drag velocity ($r_{\mathrm{b}} = \{2, 3, 4, 5, 6, 7, 8, 9, 10\} \times 10^{-4}\,\mathrm{m\,s^{-1}}$). All other model parameters are held fixed. Each experiment is "spun up" at low resolution ($N_x \times N_y = 256 \times 128$ points) for either 200 years (for $\tau_{\mathrm{w}}^{\max} \geq 0.05\,\mathrm{N\,m^{-2}}$) or 400 years (for $\tau_{\mathrm{w}}^{\max} < 0.05\,\mathrm{N\,m^{-2}}$), because experiments with weak surface wind stress require longer to reach a statistically steady state (Constantinou and Hogg 2019). We then interpolate the model state to the high-resolution grid ($N_x \times N_y = 512 \times 256$ points) and continue the spin-up for a further 100 years to re-establish statistical equilibrium; over the last 30 years integration, the linear trend in the annually-computed zonal transport is not significant at the 5% level. Finally, we continue each high-resolution run for a further 30 years, which serves as the analysis period.

b. Zonal versus along-streamline momentum balance

In Section 1 we framed the "eddy saturation" phenomenon in terms of the momentum balance of the ACC (see Figure 1). In this subsection we show (consistent with previous studies, *c.f.* Abernathey and Cessi (2014)), that in streamline-following coordinates, eddy isopycnal form

stress is almost entirely responsible for the downward transfer of momentum. Therefore, in this coordinate system the analysis of eddy saturation is simplified in that it requires consideration of only the eddy (and not the mean) isopycnal form stress term. We will take advantage of this result in Section 2c to decompose the isopycnal form stress response (which results in eddy saturation) into contributions from changes in mean and transient motions.

We now provide reference diagnostics of the mean circulation balance in our reference simulation, defined by a wind stress maximum of $\tau_w^{\max} = 0.1\,\mathrm{N\,m^{-2}}$, to match the order of magnitude of the maximum wind stress over the ACC (Large and Yeager 2009), and a quadratic bottom drag coefficient of $C_d = 2\times10^{-3}$ (Gill 1982; Arbic and Scott 2008). Figure 3 shows the time-mean momentum balance averaged zonally in both latitudinal and along-stream coordinates, and taken either over the full ocean depth or just the upper isopycnal layer. We separate "mean" versus "eddy" contributions to the momentum advection via thickness-weighted averaging (Young 2012; Aiki et al. 2016),

$$\nabla\cdot\left(\overline{h_k\boldsymbol{u}_k\boldsymbol{u}_k}\right) = \underbrace{\nabla\cdot\left(\overline{h_k}\widehat{\boldsymbol{u}}_k\widehat{\boldsymbol{u}}_k\right)}_{\text{mean advection}} + \underbrace{\nabla\cdot\left(\overline{h_k}\widehat{\boldsymbol{u}_k^\dagger\boldsymbol{u}_k^\dagger}\right)}_{\text{eddy advection}}. \tag{10}$$

Here the overbar $\overline{\bullet}$ denotes a time-average over the 30-year simulation analysis period. The hat operator denotes a thickness-weighted average, with daggers denoting fluctuations,

$$\widehat{\boldsymbol{u}}_k = \frac{\overline{h_k\boldsymbol{u}_k}}{\overline{h_k}}, \qquad \boldsymbol{u}_k^\dagger = \boldsymbol{u}_k - \widehat{\boldsymbol{u}}_k. \tag{11}$$

We separate "mean" and eddy components of the pressure gradient force (PGF) as

$$\overline{h_k\nabla M_k} = \underbrace{\overline{h_k}\nabla\overline{M_k}}_{\text{mean PGF}} + \underbrace{\overline{h_k'\nabla M_k'}}_{\text{eddy PGF}}, \tag{12}$$

where primes denote deviations from the time-average, *i.e.* $\bullet' = \bullet - \overline{\bullet}$. The resulting averaged momentum equations are given in full in Appendix A.

Figure 3(b–c) shows the zonally-averaged, time-mean zonal momentum balance. Consistent with previous studies (*e.g.* Treguier and McWilliams 1990; Abernathey and Cessi 2014; Stewart and Hogg 2017), in this coordinate system the wind-input momentum is transferred downward almost entirely via the action of mean IFS, and then removed at the sea floor via topographic form stress (TFS),

$$\underbrace{\tau_w(y)}_{\text{wind stress}} \approx \underbrace{\langle\overline{p_\eta}\partial_x\overline{\eta}\rangle_x}_{\text{mean IFS}} \approx \underbrace{\langle\overline{p_b}\partial_x\eta_b\rangle_x}_{\text{TFS}} \tag{13}$$

Here $\langle\bullet\rangle_x$ denotes a zonal average, $p_\eta = p|_{z=\eta}$ is the pressure on the isopycnal interface, and $p_b = p|_{z=\eta_b}$ is the pressure at the sea floor. Note that the forms of the IFS and TFS terms differ locally from those given in Appendix A, but are equivalent when integrated over any closed contour

$$\oint_C \rho_0 h_1\nabla M_1\cdot\mathrm{d}\boldsymbol{s} = \oint_C p_\eta\nabla\eta\cdot\mathrm{d}\boldsymbol{s}, \tag{14a}$$

$$\oint_C \rho_0\sum_k h_k\nabla M_k\cdot\mathrm{d}\boldsymbol{s} = \oint_C p_b\nabla\eta_b\cdot\mathrm{d}\boldsymbol{s}, \tag{14b}$$

where $\mathrm{d}\boldsymbol{s}$ denotes an infinitesimal line element along the closed contour C.

As noted by Abernathey and Cessi (2014), integration along lines of constant latitude obscures the role of transient eddies. Figure 3(d–e) shows the time-mean momentum balance integrated along contours of mean sea surface height, *i.e.* mean geostrophic streamlines, then divided by the zonal domain length L_x (see Appendix A). As we employ the rigid-lid approximation (see Section 2a), we define an equivalent sea surface height via the surface pressure as $\zeta = \pi/g$. In this coordinate system the mean IFS vanishes identically, and the momentum balance approximately becomes (*c.f.* Johnson and Bryden 1989)

$$\underbrace{\oint_{\overline{\zeta}=\zeta_0}\tau_w\hat{\boldsymbol{x}}\cdot\mathrm{d}\boldsymbol{s}}_{\text{wind stress}} \approx \underbrace{\oint_{\overline{\zeta}=\zeta_0}\overline{p_\eta'\nabla\eta'}\cdot\mathrm{d}\boldsymbol{s}}_{\text{eddy IFS}} \approx \underbrace{\oint_{\overline{\zeta}=\zeta_0}\overline{p_b}\nabla\eta_b\cdot\mathrm{d}\boldsymbol{s}}_{\text{TFS}}. \tag{15}$$

Here ζ_0 denotes the mean sea surface height contour along which the line integral is taken; the mean sea surface height in our reference experiment is shown in Figure 3.

c. *Separating transient eddy and mean flow contributions to eddy IFS*

As discussed in Section 1, it remains unclear to what extent "eddy saturation" occurs as a result of changes in the efficiency of transient eddies in transferring momentum downward via IFS versus adjustment of the ACC's standing meanders. To distinguish between these contributions, we relate the eddy IFS locally to the vertical gradient of the mean flow (Greatbatch and Lamb 1990), which is equivalent (in the quasi-geostrophic limit) to assuming a down-gradient horizontal buoyancy flux (Gent et al. 1995),

$$\boldsymbol{\tau}_{\text{eddy}} \equiv \overline{p_\eta'\nabla\eta'} \equiv \kappa\frac{\rho_0 f^2}{g'}\left(\widehat{\boldsymbol{u}_1} - \widehat{\boldsymbol{u}_2}\right) + \nabla D. \tag{16}$$

The first term on the right-hand-side of (16) is approximately non-divergent (under quasi-geostrophic scaling, and for slow spatial variations in κ). We make the ansatz that this term accounts for the rotational component of the eddy IFS, and allow for an additional divergent component of the eddy IFS, ∇D (see Marshall and Shutts 1981).

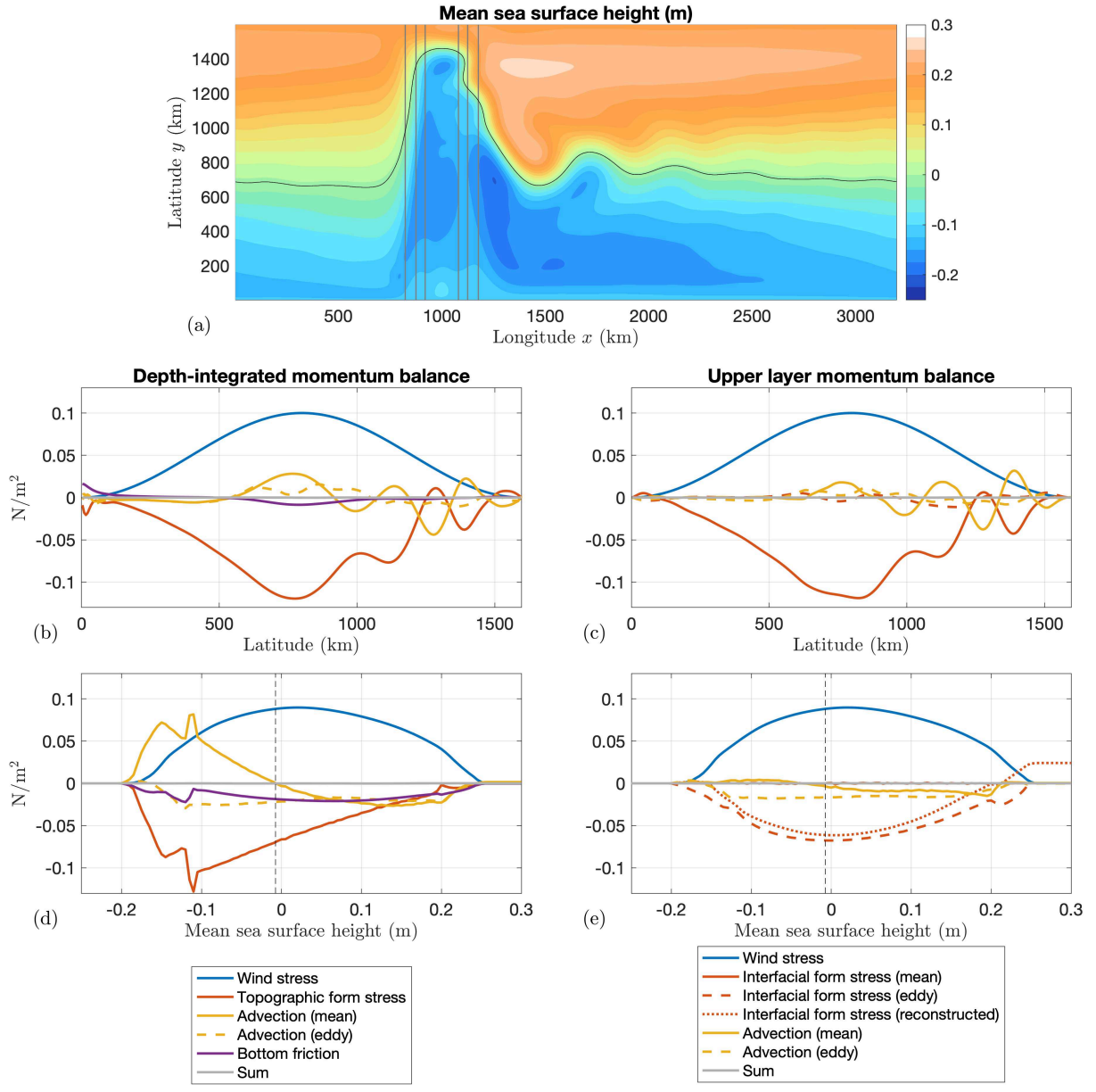

FIG. 3. Momentum balance in latitudinal vs. streamline-following coordinates. (a) Time-mean equivalent sea surface height (SSH) in our reference simulation. The black contour indicates the core of the ACC, defined to be the median value of the SSH over the entire model domain. Dark gray contours indicate the 3750 m, 3500 m and 3250 m isobaths. (b) Depth-integrated and (c) upper-isopycnal layer momentum balances, integrated along lines of constant latitude. (d) Depth-integrated and (c) upper-isopycnal layer momentum balances, integrated along contours of constant time-mean SSH. Explicit definitions of all of the terms in the momentum budget are given in Appendix A. The black dashed line in panels (b–e) corresponds to the median SSH, as shown in panel (a). The red dotted line in panel (e) is the eddy interfacial form stress reconstructed from the time-mean flow and the diagnosed eddy diffusivity κ via (17).

Substituting (16) into (15), we obtain

$$\oint_{\overline{\zeta}=\zeta_0} \boldsymbol{\tau}_{\text{eddy}} \cdot \mathrm{d}\boldsymbol{s} = \oint_{\overline{\zeta}=\zeta_0} \underbrace{\kappa}_{\substack{\text{eddy}\\ \text{efficiency}}} \cdot \underbrace{\frac{\rho_0 f^2}{g'} (\widehat{\boldsymbol{u}_1} - \widehat{\boldsymbol{u}_2}) \cdot \mathrm{d}\boldsymbol{s}}_{\text{standing meander structure}} \tag{17}$$

In Section 3 we will use (17) to quantify the contributions of transient eddies versus standing meanders in adjusting the eddy IFS to changes in wind stress. To do this, we require spatially-varying estimate of κ, which is defined implicitly by (16). We diagnose κ by taking the

curl of (16) to eliminate the divergent component of the eddy IFS,

$$\overline{J\left(p'_\eta,\eta'\right)} \approx \kappa \frac{\rho_0 f^2}{g'} \nabla \times (\widehat{\boldsymbol{u}_1} - \widehat{\boldsymbol{u}_2}) \,. \tag{18}$$

Here we have additionally neglected spatial variations of f and κ, under the assumption that they vary slowly relative to the mean flow. Although (18) could be used directly to calculate κ at each point in the model domain, $\boldsymbol{x} = \boldsymbol{x}_0$, the result is excessively noisy. Instead, we invert (18) for κ via least-squares linear regression of $\overline{J(p'_\eta,\eta')}$ on $(\rho_0 f^2/g')\nabla \times (\widehat{\boldsymbol{u}_1} - \widehat{\boldsymbol{u}_2})$ over all points within a 200 km radius of $\boldsymbol{x}_0$. The linear fits are statistically significant (p-values typically many orders of magnitude smaller than 0.001) over almost all of the model domain.

Figure 4 shows the spatial distribution of κ in our reference simulation, as compared with the distribution of the depth-averaged eddy kinetic energy (EKE),

$$\mathrm{EKE} = \frac{1}{\sum_k h_k} \sum_k \tfrac{1}{2} \overline{h_k} \widehat{\boldsymbol{u}^{\dagger 2}}. \tag{19}$$

Both the EKE and κ are elevated downstream of the bathymetric ridge, consistent with previous modeling studies and observations (*e.g.* Bischoff and Thompson 2014; Meredith 2016). This correspondence is visually evident in the "storm track" region (Bischoff and Thompson 2014), which we define as the uppermost quartile of the EKE over the entire model domain (see Figure 4(a)). In this region there is generally little scatter in the linear regression that we use to estimate κ (Figure 4(c)), supporting our assumption that κ is slowly-varying relative to the mean flow. Note that the region within 200–300 km of the northern boundary also exhibits little scatter in the linear regression, but that this is an artifact resulting from the tendency of the sponge layer to create elongated zonal structures in both $\overline{J(p'_\eta,\eta')}$ and $(\rho_0 f^2/g')\nabla \times (\widehat{\boldsymbol{u}_1} - \widehat{\boldsymbol{u}_2})$.

To further evaluate our approach to estimating κ, we compute the alongstream-averaged eddy IFS via (17). Figure 3(e) shows that this reconstruction only slightly underestimates the diagnosed alongstream-averaged eddy IFS, by around 10–20% over the SSH contours that cross the bathymetric ridge (see Figure 3(a)).

3. Saturation by transient eddies versus standing waves

In this section we utilize our suite of model experiments (see Section 2a) to assess the extent to which adjustment of transient eddy behavior versus mean flow structure is responsible for "eddy saturation". Briefly, we first show that the model's baroclinic transport is indeed saturated in experiments with varying zonal wind stress, consistent with previous studies. We then show that the diagnosed variations in the transient eddy diffusivity (along with the eddy kinetic energy) suggests that transient eddies are not adjusting sufficiently rapidly to support the transport saturation. Finally, we use our decomposition of the eddy IFS (17) to verify that the saturation occurs primarily via adjustments of the standing waves, rather than of the transient eddies.

To evaluate the extent to which our idealization of the ACC is "eddy saturated", we examine the sensitivity of both the total transport and its barotropic/baroclinic components, defined respectively as

$$T_{\mathrm{tot}} = \left\langle \int_0^{L_y} \sum_k \overline{h_k u_k} \right\rangle_x , \tag{20a}$$

$$T_{\mathrm{bt}} = \left\langle \int_0^{L_y} u_2 \sum_k \overline{h_k} \right\rangle_x , \tag{20b}$$

$$T_{\mathrm{bc}} = T_{\mathrm{tot}} - T_{\mathrm{bt}}. \tag{20c}$$

We define the lower-layer flow as the barotropic component of the zonal flow, and then average the associated barotropic transport zonally to obtain T_{bt}, with T_{bc} computed as a residual.

In Figure 5 we plot the dependence of these transports on the wind stress maximum and the quadratic drag coefficient. The total volume transport is generally substantially lower than the observed transport of the ACC (Whitworth and Peterson 1985; Donohue et al. 2016), but is of the correct order of magnitude, and is comparable to previously-reported transports in channel model simulations (*e.g.* Stewart and Hogg 2017; Youngs et al. 2019). Fig 5 shows that the baroclinic transport is approximately independent of wind stress, whereas the barotropic transport increases with wind stress, and thus so does the total transport. This is consistent with some previous modeling studies (Nadeau and Ferrari 2015; Youngs et al. 2019), whereas others have found that the total transport is approximately independent of the wind stress (Munday et al. 2013; Marshall et al. 2017). Similar to Marshall et al. (2017), the total, barotropic and baroclinic transports all increase with quadratic drag coefficient, although for drag coefficients $\gtrsim 2 \times 10^{-3}$ this sensitivity is relatively weak. For the strongest wind stresses and weakest bottom friction coefficients examined here, the barotropic transport actually begins to decrease with wind stress, and may even become negative. This flow reversal appears to be associated with extreme strengthening of deep gyres in the lee of the ridge (Nadeau and Ferrari 2015), but the specific mechanism via which it occurs and its relevance to the dynamics of the ACC are left as a topic for future investigation.

To obtain preliminary insights into how transient eddies and standing meanders/waves change while preserving the baroclinic flow, we now examine the response of the transient eddy and standing wave activity to variations in the wind stress. Figure 6(a) shows the sensitivity of κ,

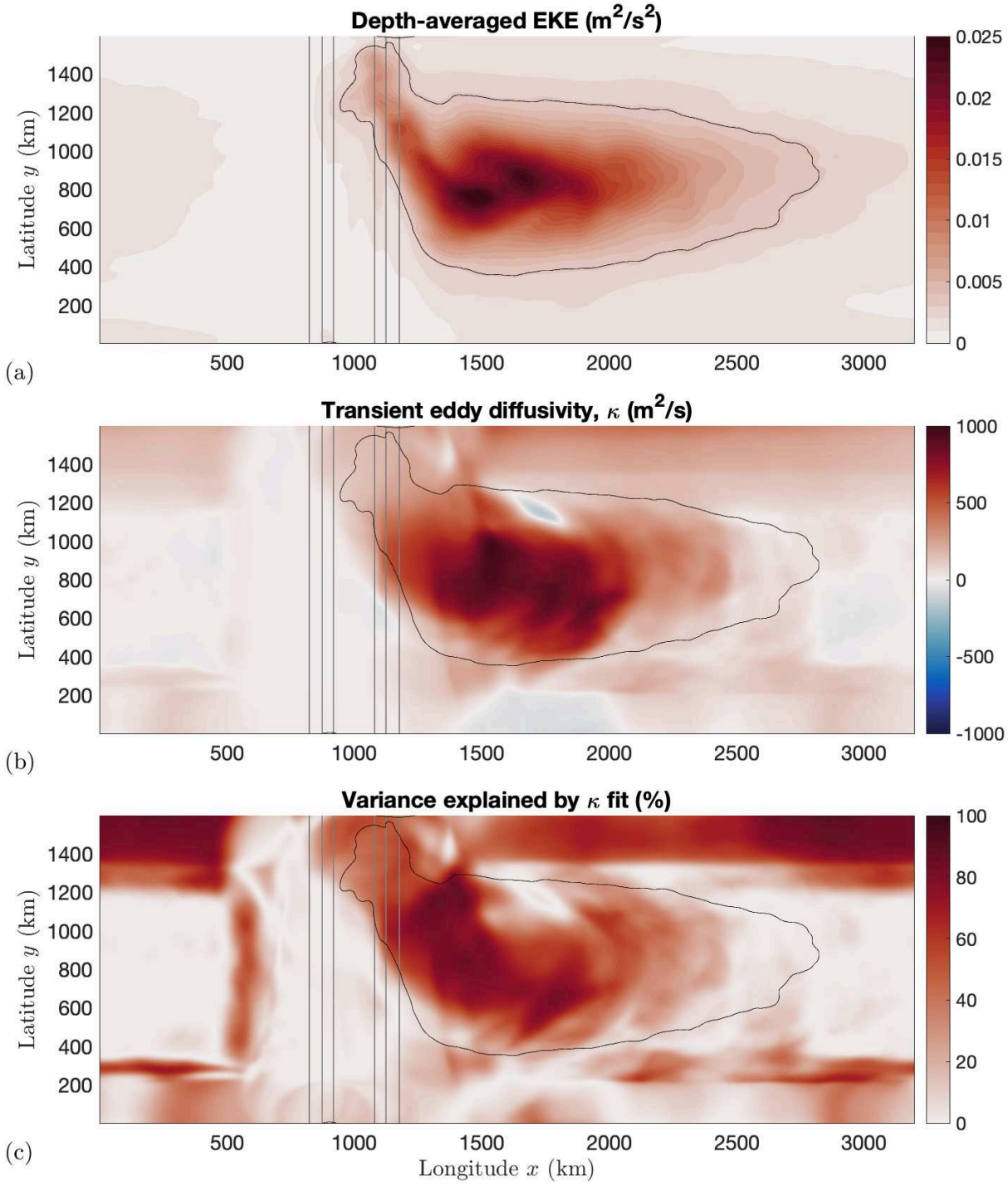

FIG. 4. Diagnostics of eddy activity in our reference simulation. (a) Depth-averaged eddy kinetic energy (EKE), (b) estimated transient eddy diffusivity, and (c) variance explained by our linear regression-based estimate of κ (see Section 2c). In all panels the black contour bounds the fourth quartile of the EKE, which defines our "storm track" region. The gray contours indicate the 3750 m, 3500 m and 3250 m isobaths.

spatially averaged over the "storm track" region in each simulation, to changes in the wind stress maximum and quadratic drag coefficient. Least squares logarithmic fits over all of our simulations yield approximate scalings of

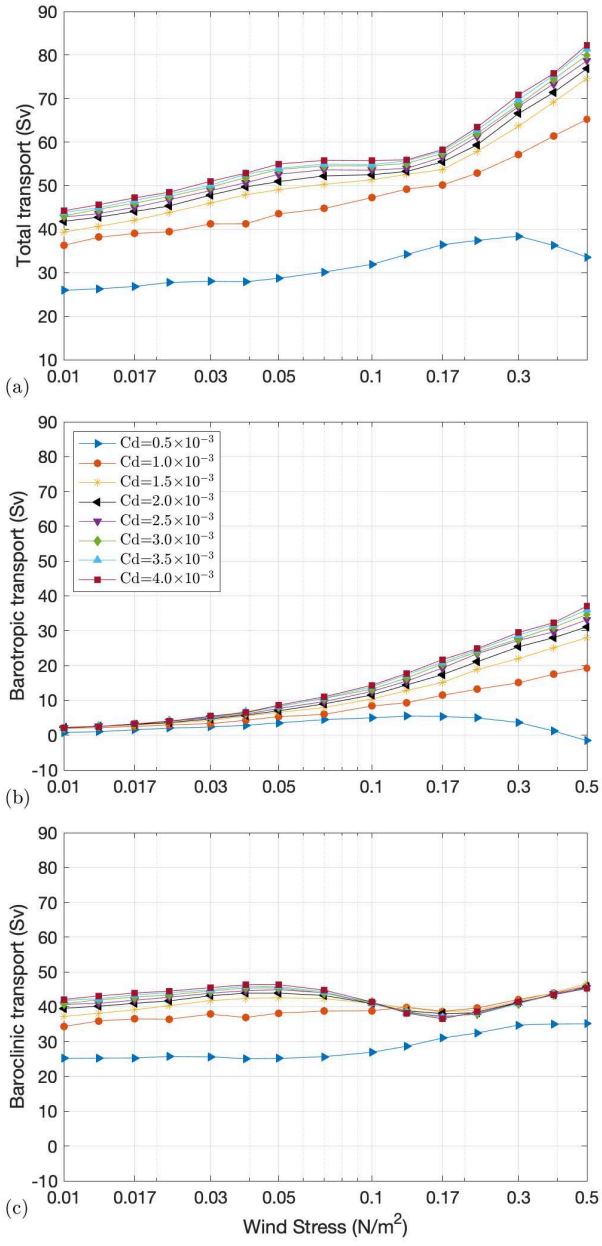

FIG. 5. Dependence of the (a) total transport, (b) barotropic transport and (c) baroclinic transport on the wind stress maximum and on the quadratic drag coefficient in our channel model simulations. Note the nonlinear abscissa.

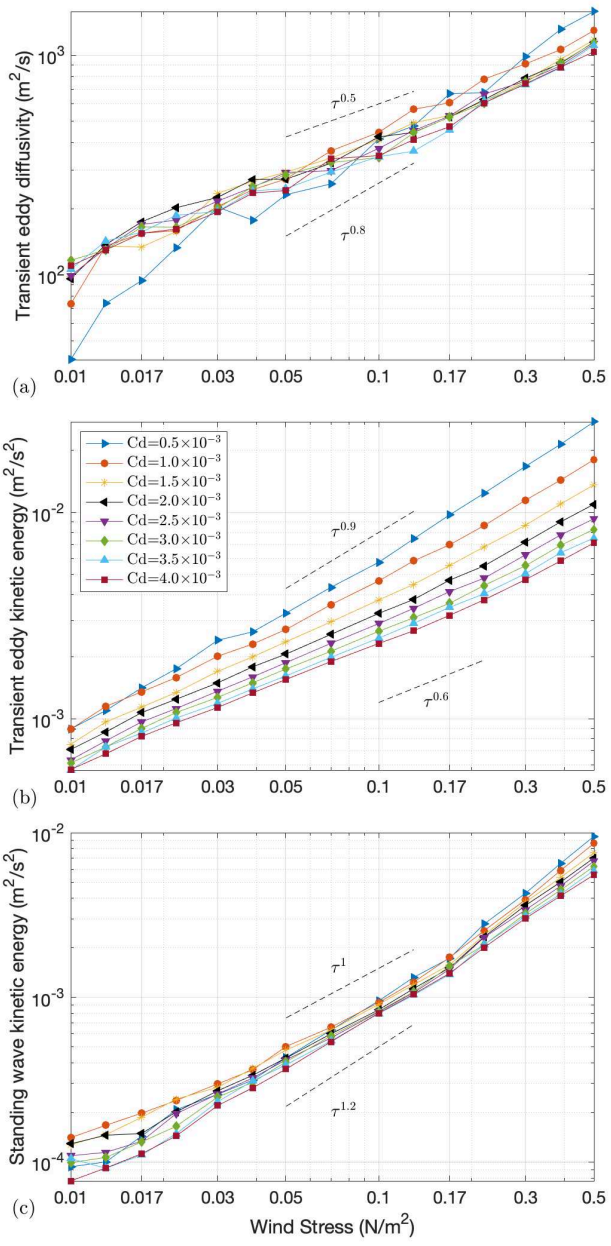

FIG. 6. Sensitivity of transient eddies and standing waves to the wind stress maximum and the quadratic drag coefficient. (a) Transient eddy diffusivity κ averaged over the "storm track" region (see Figure 4), (b) domain-averaged eddy kinetic energy, and (c) domain-averaged standing wave energy.

$\kappa \sim \tau_w^{0.6}$ and EKE $\sim \tau_w^{0.7}$. Including random multiplicative errors with average magnitudes of 10% in the estimate of κ, motivated by our comparison between the diagnosed and reconstructed eddy IFS in Figure 2, does not change the scaling of κ with τ_w to within one decimal place. In contrast, residual-mean theory (Marshall and Radko 2003) predicts that κ must scale linearly with τ_w in order to preserve the baroclinic transport. Thus our diagnostics suggest that adjustments in the efficiency of downward transient eddy momentum transfer (*i.e.* of κ) are not sufficient to produce the "eddy saturation" response in these simulations. Figure 6(c) shows the sensitivity of the domain-averaged standing wave kinetic energy (SKE), which we simply es-

timate as the depth-averaged mean kinetic energy,

$$\mathrm{SKE} = \frac{1}{\sum_k h_k} \sum_k \tfrac{1}{2} \overline{h_k} \widehat{\boldsymbol{u}_k}^2. \tag{21}$$

In contrast to the EKE, the SKE scales approximately linearly with wind stress, with $\mathrm{SKE} \sim \tau^{1.1}$. This is qualitatively consistent with "flexing" of the standing meander in response to increased zonal wind stress (Thompson and Naveira Garabato 2014), though the change in SKE could also arise due to spin-up of the mean gyres that abut the circumpolar flow in Figure 3 (Nadeau and Ferrari 2015).

To quantify the relative roles of transient eddy versus standing wave adjustment in "eddy saturation", we now separately examine their contributions to the changes in eddy IFS that occur in response to wind stress perturbations. The rationale for this approach is that the wind-input momentum along mean streamlines is primarily transferred downward toward the sea floor via eddy IFS, (*c.f.* Equation (15)). To demonstrate that this holds across the parameter space examined in this study, in Figure 7(a) we quantify the contributions of wind stress, eddy IFS and eddy advection (*c.f.* Figure 3) to the along-stream momentum balance. We plot these contributions as functions of the wind stress maximum, holding the quadratic drag coefficient fixed at $C_d = 2 \times 10^{-3}$. For each simulation we select a mean streamline that tracks the core of the zonally re-entrant flow by taking the median of the time-mean SSH over the entire model domain, *e.g.* as shown in Figure 3(a). For all of the wind stresses examined here, the upper-layer momentum balance along this contour is primarily between the wind stress and the eddy IFS, although horizontal redistribution of momentum by eddies balances up to 25% of the wind stress. We therefore conclude that (15) holds approximately across our suite of simulations.

To quantify the contributions of transient eddies versus standing waves to changes in eddy IFS, we use (15) to produce estimates of the eddy IFS resulting from independent perturbations of κ and the mean flow, respectively. For notational clarity we first rewrite (17) as

$$\mathrm{EIFS} = \mathcal{F}[\kappa, \overline{\boldsymbol{u}}], \tag{22}$$

where EIFS denotes the alongstream-averaged eddy IFS, the functional $\mathcal{F}$ is defined by the right-hand side of (17), and $\overline{\boldsymbol{u}}$ is shorthand for the time-mean flow in both isopycnal layers. We then define reference spatial distributions of κ and $\overline{\boldsymbol{u}}$ from our reference experiment (see Section 2b), which we denote as κ_{ref} and $\overline{\boldsymbol{u}}_{\mathrm{ref}}$ respectively. Finally, for each of our experiments we define two reconstructions of the eddy IFS,

$$\mathrm{EIFS}|^{(n)}_{\kappa=\kappa_{\mathrm{ref}}} = \mathcal{F}\left[\kappa_{\mathrm{ref}}, \overline{\boldsymbol{u}}^{(n)}\right], \tag{23a}$$

$$\mathrm{EIFS}|^{(n)}_{\overline{\boldsymbol{u}}=\overline{\boldsymbol{u}}_{\mathrm{ref}}} = \mathcal{F}\left[\kappa^{(n)}, \overline{\boldsymbol{u}}_{\mathrm{ref}}\right]. \tag{23b}$$

Here $^{(n)}$ is an arbitrary index to distinguish different experiments, and $\kappa^{(n)}$ and $\overline{\boldsymbol{u}}^{(n)}$ denote the eddy diffusivity and mean flow diagnosed from the n^{th} experiment. Thus the reconstructions $\mathrm{EIFS}|^{(n)}_{\kappa=\kappa_{\mathrm{ref}}}$ provide an estimate of the eddy IFS response that results from varying only the mean flow, while the reconstructions $\mathrm{EIFS}|^{(n)}_{\overline{\boldsymbol{u}}=\overline{\boldsymbol{u}}_{\mathrm{ref}}}$ provide an estimate of the eddy IFS response that result from varying only the eddy diffusivity.

Figure 7(b) demonstrates this approach, focusing on the same subset of our simulations as shown in Figure 7(a). Holding the mean flow fixed and varying κ yields a reconstructed eddy IFS that increases with the wind stress, but with a substantially smaller slope than the diagnosed eddy IFS. In particular, for wind stresses larger than the reference value, the reconstructed eddy IFS is almost invariant under increases of the wind stress. This implies that changes in transient eddy diffusivity alone fail to capture the "eddy saturation" response. In contrast, holding κ fixed and varying the mean flow yields a reconstructed eddy IFS that closely tracks the diagnosed IFS.

Figures 7(c) and (d) expand the scope of this analysis to include our entire suite of simulations with varying wind stress maximum and quadratic drag coefficient. These reconstructions exhibit the same qualitative pattern as Figure 7(b), despite significant scatter associated with the varying quadratic drag coefficient. To provide a quantitative assessment of these reconstructions, we note that the eddy IFS spans orders of magnitude, and thus we quantify the root-mean-square difference between the logarithms of the diagnosed and reconstructed eddy IFS (the LRMSE). Consistent with our inference based on visual inspection, the LRMSE of $\mathrm{EIFS}|^{(n)}_{\overline{\boldsymbol{u}}=\overline{\boldsymbol{u}}_{\mathrm{ref}}}$ is substantially higher than that of $\mathrm{EIFS}|^{(n)}_{\kappa=\kappa_{\mathrm{ref}}}$ ($\sim$0.30 versus $\sim$0.14). These diagnostics indicate that the "eddy saturation" response occurs primarily as a result of adjustment of the mean flow, *i.e.* of the standing meander, rather than of the efficiency of eddy momentum transfer.

4. A theory of standing wave saturation

The diagnostics presented in Section 3 indicate that "eddy saturation" occurs primarily as a result of adjustment of standing meanders in response to changes in zonal wind stress. Motivated by this finding, we now pose a quasi-geostrophic standing wave theory of eddy saturation. This theory simultaneously supports the conclusions drawn from our simulations and yields insight into the dynamics of eddy saturation.

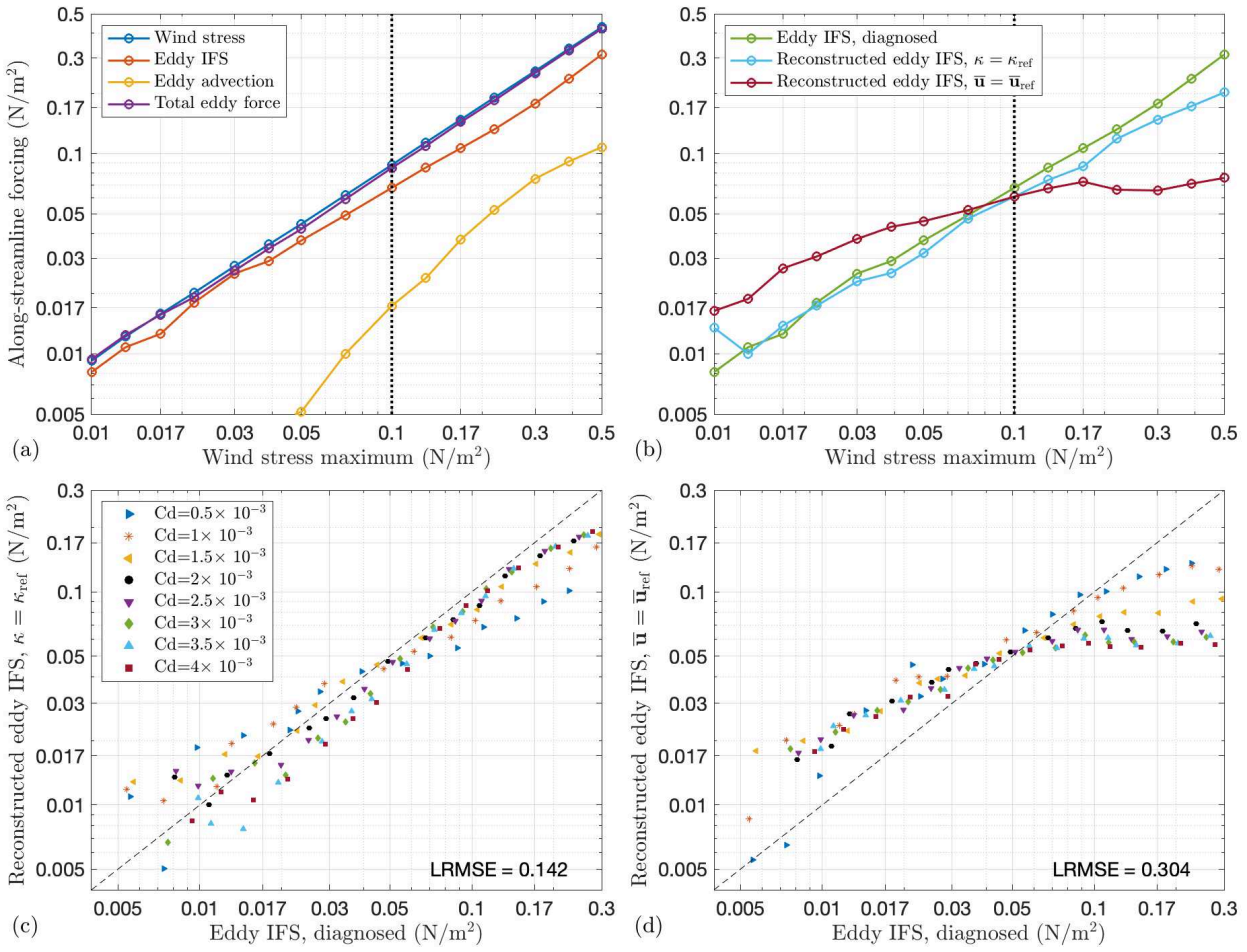

FIG. 7. (a) Upper-layer momentum budget along a streamline through the core of the circumpolar flow (see Figure 3(a,e)) in experiments with varying wind stress maxima $\tau_{\rm w}^{\rm max}$ and fixed quadratic drag coefficient $C_{\rm d} = 2\times10^{-3}$. The "total eddy force" is the sum of the eddy IFS and eddy momentum flux convergence. (b) Reconstructions of the eddy IFS obtained via (17) in which we independently vary the mean flow while holding the spatial distribution of κ fixed and equal to that of the reference simulation, $\kappa_{\rm ref}$ (blue points); and varying κ while holding the mean flow $\overline{\boldsymbol{u}}$ fixed and equal to that of the reference simulation, $\overline{\boldsymbol{u}}_{\rm ref}$ (red points). The quadratic drag coefficient is held fixed and equal to $C_{\rm d} = 2\times10^{-3}$. (c) Reconstruction of the eddy IFS via (17) across our entire suite of simulations with fixed κ and varying mean flow. (d) As (c), but with fixed mean flow and varying κ.

a. Theoretical model formulation

Our theoretical model closely follows those derived in several recent studies (Abernathey and Cessi 2014; Constantinou and Young 2018; Bai et al. 2021), which in turn build on earlier work by Davey (1980). Under the assumptions that the flow is quasi-geostrophic and slowly-varying in the meridional direction, this formulation simplifies conservation of potential vorticity to a one-dimensional wave equation, complemented by a zonal momentum equation that constrains the zonal mean flow. The resulting system can, in principle, be solved analytically to produce explicit predictions of the circumpolar transport and the structures of the standing meanders/waves. Below we discuss the key steps required to derive the model equations, and then discuss our method of solution.

We start with the 2-layer quasi-geostrophic analogue of (2)–(4) (*e.g.* Pedlosky 1987), neglecting diapycnal fluxes and the hyperviscous stress tensor. Taking a time average, these equations become

$$\frac{\partial \overline{q_k}}{\partial t} + J\left(\overline{\psi_k}, \overline{q_k}\right) + \nabla\cdot\overline{\boldsymbol{u}_k' q_k'} = -\frac{\delta_{1,k}}{\rho_0 H_1}\frac{\partial \tau_{\rm w}}{\partial y} - \frac{\delta_{2,k}}{\rho_0 H_2}\nabla\times\overline{\boldsymbol{\tau}_{\rm b}} \tag{24}$$

where the potential vorticity (PV) in each layer is given by

$$q_k = \nabla^2\psi_k + \beta y + (-1)^k L_k^{-2}(\psi_1 - \psi_2) + \delta_{2,k}\frac{f_0}{H_2}\eta_b. \tag{25}$$

Here ψ_k is the geostrophic streamfunction, $\boldsymbol{u}_k = -\nabla\times\psi_k\hat{\boldsymbol{z}}$ is the geostrophic velocity, $J(\bullet,\bullet)$ denotes the Jacobian operator, the deformation radius in each layer is defined as $L_k = \sqrt{g'H_k}/|f_0|$, and the reference layer thicknesses are $H_1 = 1500\,\mathrm{m}$ and $H_2 = 2500\,\mathrm{m}$. Unless otherwise stated, the model parameters and geometry match those given in Section 2a. In order to make the theory analytically tractable, we use the linear formulation (7) of the bottom frictional stress.

The transient eddy PV flux in (24) can be decomposed, following some manipulations, as

$$\nabla\cdot\overline{\boldsymbol{u}_k'q_k'} = \underbrace{\nabla\cdot\overline{\boldsymbol{u}_k'\xi_k'}}_{\text{vorticity flux divergence}} + \underbrace{(-1)^{(k-1)}L_k^{-2}\overline{J(\psi_1',\psi_2')}}_{\text{isopycnal pressure torque}}, \tag{26}$$

where $\xi_k = \nabla\times\boldsymbol{u}_k = \nabla^2\psi_k$ is the relative vorticity. Following (18), we assume that the isopycnal pressure torque acts down the vertical gradient of the relative vorticity, *i.e.*

$$\frac{f_0^2}{g'}\overline{J(\psi_1',\psi_2')} = \frac{f_0^2}{g'}\kappa\left(\overline{\xi_1}-\overline{\xi_2}\right), \tag{27}$$

where κ is taken to be a constant. We further assume that the horizontal fluxes of relative vorticity are also directed down the mean relative vorticity gradient,

$$\overline{\boldsymbol{u}_k'\xi_k'} = -\nu\nabla\overline{\xi}_k, \tag{28}$$

where ν is a constant horizontal eddy viscosity. Bai et al. (2021) showed that adding a horizontal eddy viscosity to a barotropic standing wave model removes the indeterminacy of the solution that occurs when dissipation can only occur via bottom friction (see also Constantinou and Young 2018). Substituting (26)–(28) and (7) into (24) yields the following evolution equation for the mean PV,

$$\frac{\partial\overline{q_k}}{\partial t} + J\left(\overline{\psi_k},\overline{q_k}\right) = \nu\nabla^2\overline{\xi_k} + (-1)^k L_k^{-2}\kappa(\overline{\xi_1}-\overline{\xi_2}) - \frac{\delta_{1,k}}{\rho_0 H_1}\frac{\partial\tau_\mathrm{w}}{\partial y} - \frac{\delta_{2,k}r_b}{\rho_0 H_2}\overline{\xi_2}. \tag{29}$$

We now partition the mean streamfunction into a zonal mean component $\langle\overline{\psi_k}\rangle_x(y,t)$ and perturbation component $\tilde{\psi}_k(x,y,t)$,

$$\overline{\psi_k} = \langle\overline{\psi_k}\rangle_x + \tilde{\psi}_k, \tag{30}$$

and we define the zonal-mean zonal velocity in each layer as $U_k = -\partial_y\langle\overline{\psi_k}\rangle_x$. We then assume that the time-averaged system is in steady state, *i.e.* $\partial_t \equiv 0$, and that the flow is slowly varying in y, *i.e.* $\partial_y \ll \partial_x$, such that all derivatives of $\tilde{\psi}_k$ and U_k with respect to y can be neglected. After further manipulations, (29) may be rewritten in the form of a linear wave equation,

$$U_k\partial_x^3\tilde{\psi}_k + L_k^{-2}(-1)^k\left(U_2\partial_x\tilde{\psi}_1 - U_1\partial_x\tilde{\psi}_2\right) + \beta\partial_x\tilde{\psi}_k + \delta_{2,k}U_2\frac{f_0}{H_2}\partial_x\eta_b = -\delta_{2,k}\frac{r_b}{H_2}\partial_x^2\tilde{\psi}_2 + \nu\partial_x^4\tilde{\psi}_k + (-1)^k\kappa L_k^{-2}\partial_x^2\left(\tilde{\psi}_1-\tilde{\psi}_2\right). \tag{31}$$

We derive the corresponding zonal momentum equations by multiplying (29) by H_k, integrating from $y' = 0$ to $y' = y$ and zonally averaging, where y' is a variable of integration. Assuming that the meridional velocity and wind/frictional stresses are zero at $y = 0$, this yields

$$\tau_\mathrm{w} = \mathrm{EIFS} + \mathrm{SIFS}, \tag{32a}$$

$$\mathrm{EIFS} + \mathrm{SIFS} = \mathrm{TFS} + \rho_0 r_\mathrm{b} U_2, \tag{32b}$$

where

$$\mathrm{SIFS} = \frac{\rho_0 f_0^2}{g'}\left\langle\tilde{\psi}_1\partial_x\tilde{\psi}_2\right\rangle_x, \tag{33a}$$

$$\mathrm{EIFS} = \frac{\rho_0\kappa^{(y)}f_0^2}{g'}(U_1-U_2), \tag{33b}$$

$$\mathrm{TFS} = \rho_0 f\left\langle\tilde{\psi}_2\partial_x\eta_b\right\rangle_x, \tag{33c}$$

are the standing wave interfacial form stress (SIFS), eddy interfacial form stress (EIFS) and topographic form stress (TFS), respectively. Taken together, (31) and (32a)–(32b) comprise four equations for the four unknowns: the zonal mean velocities U_k and the perturbation streamfunctions $\tilde{\psi}_k$.

Note that we use a distinct eddy diffusivity, $\kappa^{(y)}$, in (33b), from that appearing in (31). The rationale for this is that (32a)–(32b) describe the zonal momentum balance zonally averaged along latitude lines, rather than the momentum balance averaged along mean streamlines. Based on our simulations (see Figure 3), we therefore expect the SIFS, rather than the EIFS, to balance the wind stress in (32a). In our simulations, the eddy diffusivity obtained by zonally averaging eddy IFS and zonal velocity (*c.f.* Equation (16)) across a latitude band is much smaller than the diffusivities diagnosed following the method discussed in Section 2c. Based on the diagnostics presented in Appendix C, we select $\kappa^{(y)} = 80\,\mathrm{m^2\,s^{-1}}$, whereas based on Figure 4(a), we select $\kappa = 400\,\mathrm{m^2\,s^{-1}}$. If we were to choose $\kappa^{(y)}$ to be as large as κ then we would find that EIFS made an $O(1)$ contribution to the theoretical momentum balance (not shown), conflicting with our simulation results (Figure 3). The eddy viscosity of $\nu = 2000\,\mathrm{m^2\,s^{-1}}$ is chosen to be as small as possible while preserving the stability of our numerical solutions, discussed below.

Although in principle analytical progress toward a solution of (31)–(33c) can be achieved via a zonal Fourier

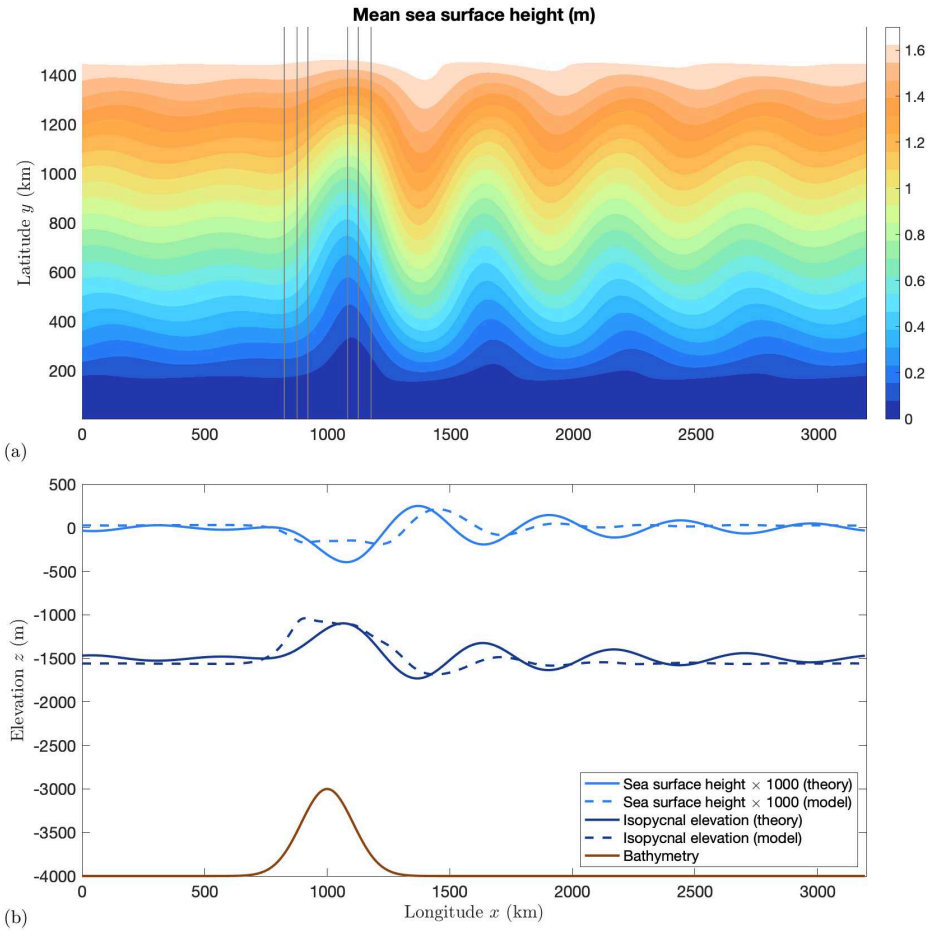

FIG. 8. (a) Equivalent sea surface height predicted by our quasi-geostrophic standing wave theory (see Section 4a). Dark gray contours indicate the 3750 m, 3500 m and 3250 m isobaths. Note the different color axis range from Figure 3(a). (b) Comparison of the theoretically predicted sea surface height (amplified by a factor of 1000 for visibility) and isopycnal interface elevation along $y = L_y/2$ with those diagnosed from our reference simulation.

transform (Bai et al. 2021), in practice the resulting equations yield little additional physical insight. We therefore solve the equations numerically via Matlab's least-squares Trust-Region Reflective algorithm. In all cases presented here, the optimized solution yielded a differences between the left- and right-hand-sides of (32a)–(32b) of no more than $10^{-7}\,\mathrm{N\,m^{-2}}$, which is five orders of magnitude smaller than our smallest wind stress.

In Figure 8(a) we plot the equivalent sea surface height predicted by our theory, for comparison with the time-mean simulated sea surface height shown in Figure 3(a). In Figure 8(b) we directly compare the predicted and diagnosed sea surface height and isopycnal elevation along the mid-line of the channel, $y = L_y/2$. Here we have solved (31)–(33c) using the corresponding wind stress at each latitude (*c.f.* Equation (5)). We use the same reference wind stress maximum as in Section 2a ($\tau_w^{\max} = 0.1\,\mathrm{N\,m^{-2}}$) and set the linear friction velocity to $r_b = 4\times10^{-4}\,\mathrm{m\,s^{-1}}$. All other model parameters are assumed to be independent of latitude. The resulting mean flow resembles a standing meander in the lee of the bathymetric ridge, but exhibits qualitative differences from the mean flow in our simulations. Notably, although the amplitude of the standing wave is similar over the ridge, the theoretical standing wave visibly persists over a longer zonal distance. The theoretical zonal-mean upper-layer flow is also larger, as indicated by the larger meridional sea surface height gradient in Figure 8 than in Figure 3. These differences likely arise because, under the assumption of a flow that is slowly-varying in y, the theoretical solution is not constrained by the meridional walls. Furthermore, the theoretical solution cannot form "gyres" in the lee of the ridge (Nadeau and Ferrari 2015), and thus the topographic form stress must be established entirely by the standing Rossby wave. The

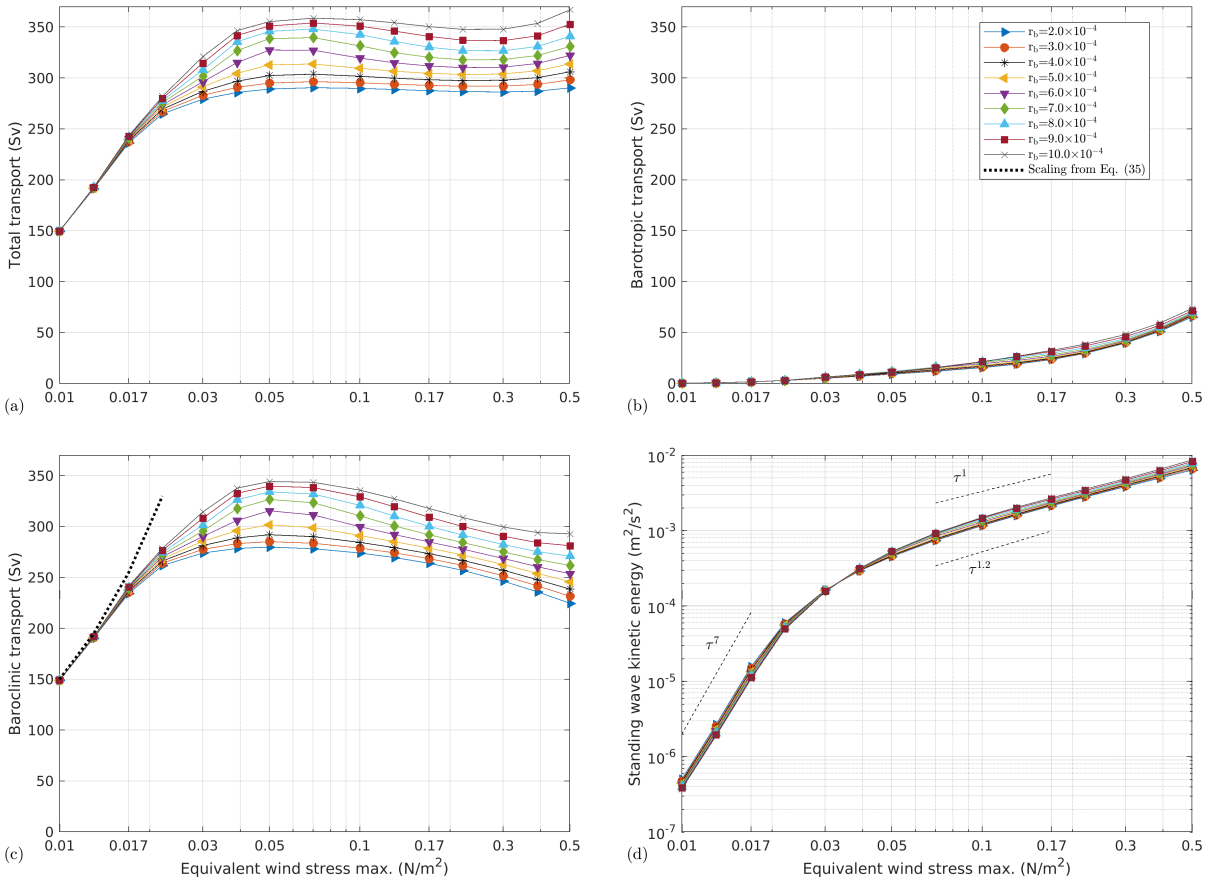

FIG. 9. Dependence of the (a) total transport, (b) barotropic transport (c) baroclinic transport, and (d) standing wave kinetic energy on the wind stress maximum and on the linear friction velocity in our quasi-geostrophic theory. Each point corresponds to a solution of Equations 31–(33c). The "equivalent wind stress maximum" defines the wind stress profile via (5), which is then meridionally averaged and used to force the theoretical momentum equation (32a). Note the nonlinear abscissa on all axes, and the nonlinear ordinate in panel (d).

theoretical baroclinic and barotropic transports are approximately 242 Sv and 15 Sv, respectively. These transports are of the same orders of magnitude as those measured in the ACC (Donohue et al. 2016) but several times higher than the corresponding transports from our simulations (see Figure 5). We conclude that our theoretical solution qualitatively resembles the circulation of the ACC and produces a zonal transport of the same order of magnitude as observations, but that caution is required in comparing its predictions with the channel model simulations presented in Section 2–3.

b. Regimes of standing wave saturation

We now show that our theory captures the "eddy saturation" phenomenon, and exploit its analytical simplicity to draw some insights into the dynamics of the saturation response. We obtain solutions of (31)–(33c) over the same range of wind stresses and linear friction velocities as discussed in Section 2a. To aid our dynamical interpretation, rather than solve the theoretical model equations at all latitudes in our model domain, we instead solve the equations at a single latitude using the meridionally-averaged wind stress. For the wind stress profile (5), this corresponds to setting

$$\tau_w = \tfrac{1}{2}\tau_w^{\max} \tag{34}$$

in Eq. (32a). Thus the resulting solutions should be thought of as an approximation to the meridionally-averaged standing wave behavior, although there are substantial qualitative departures of the theoretical solutions from our simulations, as discussed in Section 4a. To obtain equivalent zonal transports, we multiply the depth-integrated mean zonal velocity (*i.e.* $H_1U_1 + H_2U_2$) by $L_y = 1600\,\text{km}$.

In Figure 9 we plot the sensitivity of the total transport, baroclinic transport, barotropic transport, and standing wave kinetic energy to changes in wind stress and

friction velocity, analogous to Figures 5 and 6(c). For wind stresses $\gtrsim 0.03\,\mathrm{N\,m^{-2}}$, the total zonal transport is approximately independent of the wind stress; this contrasts with our simulations, in which the baroclinic transport is independent of the wind stress. In this regime there is a relatively small increase in the barotropic transport with wind stress, accompanied by a compensating decrease in baroclinic transport. We note that the theory overpredicts that barotropic transport only by a factor of ∼2 (compare Figures 9(b) and 5(b)), whereas it overpredicts the baroclinic transport by a factor of ∼7 (compare Figures 9(c) and 5(c)). This discrepancy is likely related to the assumption of small meridional gradients in the theory, which eliminates the influence of meridional walls and precludes the formation of gyres in the lee of the ridge, as discussed in Section 4a.

The theoretically-predicted total and baroclinic transports increase with the linear drag coefficient, with the total transport increasing from ∼285 Sv for $r_\mathrm{b} = 2\times10^{-4}\,\mathrm{m\,s^{-1}}$ to ∼350 Sv for $r_\mathrm{b} = 1\times10^{-3}\,\mathrm{m\,s^{-1}}$. Thus the theory appears to capture the "frictional control" of the zonal transport exhibited in our simulations and previous work (Marshall et al. 2017), despite mesoscale eddies being entirely parameterized. In the eddy-saturated regime the standing wave kinetic energy increases approximately linearly with the wind stress, consistent with our simulations (see Figure 6(d)). For wind stresses $\lesssim 0.03\,\mathrm{N\,m^{-2}}$, the total and barotropic transports both increase linearly with the wind stress, while the standing wave kinetic energy rapidly decays to zero as $\tau_\mathrm{w} \to 0$, approximately scaling as $\mathrm{SKE} \sim \tau_\mathrm{w}^7$.

To aid in the interpretation of these results, in Figure 10 we plot the SIFS and TFS terms from (32a)–(32b), normalized by the wind stress. Panel a shows that in all of these solutions, TFS is almost entirely responsible for removing the wind-input momentum at the sea floor; with bottom friction (rightmost term in (32b)) playing a negligible role (*c.f.* Munk and Palmén 1951). Note that in Fig. 10, the contribution of bottom friction to the momentum balance is given by one minus the "total" curve, *i.e.* $(1 - \mathrm{TFS}/\tau_\mathrm{w})$. This should not be confused with the contribution of bottom friction to establishing the TFS, which is plotted in yellow and discussed in the following subsection. In the saturated regime ($\tau_\mathrm{w}^\mathrm{max} \gtrsim 0.03\,\mathrm{N\,m^{-2}}$) the wind stress is primarily balanced by SIFS; this is to be expected based on our model simulations, because our theoretical momentum balance is averaged along latitude lines (see Figure 3). Thus, provided that the standing waves are primarily responsible for the downward transfer of wind-input momentum, *i.e.*

$$\tau_\mathrm{w} \approx \mathrm{SIFS} \approx \mathrm{TFS}, \tag{35}$$

the theoretical model solutions exhibit saturation of the zonal transport.

Figures 10(a) and 10(b) shows that both saturation and the approximate momentum balance (35) fail for small wind stresses ($\tau_\mathrm{w}^\mathrm{max} \lesssim 0.04\,\mathrm{N\,m^{-2}}$) because the wind stress becomes balanced by EIFS instead of SIFS. The approximate wind stress required for this to occur can be estimated by computing the EIFS associated with the baroclinic shear in the saturated regime, *i.e.* $U_1 - U_2 \sim 0.1\,\mathrm{m\,s^{-1}}$, which yields $\mathrm{EIFS} = \mathrm{EIFS}^\mathrm{sat} \approx 0.008\,\mathrm{N\,m^2}$. Figure 9(b) shows that this EIFS is small compared with the SIFS in the saturated regime, but for a sufficiently small wind stress we will reach a situation where $\tau^\mathrm{w} \sim \mathrm{EIFS}^\mathrm{sat}$. When this occurs, SIFS can no longer primarily balance the wind stress and/or the baroclinic shear must decrease. To obtain an estimate for the wind stress at which this transition occurs, we use (32a) to predict that the EIFS will balance 50% of the wind stress when $\frac{1}{2}\tau_\mathrm{w} \approx \mathrm{EIFS}^\mathrm{sat} \approx 0.016\,\mathrm{N\,m^{-2}}$, *i.e.* for $\tau_\mathrm{w}^\mathrm{max} \approx 0.032\,\mathrm{N\,m^{-2}}$. This prediction agrees approximately with Figure 9(b). In this regime the transport is not saturated; instead, there is a linear dependence of the transport on wind stress (Figure 9(a)). This occurs because we have held the meridional eddy diffusivity, $\kappa^{(y)}$, constant. Assuming that $\mathrm{EIFS} \approx \tau_\mathrm{w}$ in the limit of small wind stress, we expect the baroclinic shear to scale as

$$U_1 - U_2 \to \frac{g'}{f_0^2 \rho_0 \kappa^{(y)}}\tau_\mathrm{w} \qquad \text{as} \qquad \tau_\mathrm{w} \to 0. \tag{36}$$

Figure 9 shows that this scaling accurately captures the total and baroclinic transports predicted by our theory in the limit of weak wind stress.

c. Dynamics of standing wave saturation

The above analysis demonstrates that saturation of the zonal transport can indeed occur entirely via adjustments of standing waves, as suggested by our diagnostics in Section 3. However, even from this heavily simplified theory one can not trivially discern what sets the zonal transport, nor mechanistically how the standing waves adjust such that the SIFS compensates changes in the wind stress. To yield further insight into this process, we use the standing wave energy budget to relate the SIFS and TFS to energy dissipation, building on earlier work by Abernathey and Cessi (2014). Multiplying the upper-layer wave equation (Equation (31) with $k = 1$) by $\partial_x\tilde{\psi}_1$ and zonally averaging, we obtain, after some manipulations,

$$\mathrm{SIFS} = \underbrace{\frac{\rho_0 \nu H_1}{U_1}\left\langle \left(\partial_x^2\tilde{\psi}_1\right)^2 \right\rangle_x}_{\text{viscous}} + \underbrace{\frac{\rho_0 \kappa f^2}{g' U_1}\left[\left\langle \left(\partial_x\tilde{\psi}_1\right)^2 \right\rangle_x - \left\langle \partial_x\tilde{\psi}_2 \partial_x\tilde{\psi}_1 \right\rangle_x\right]}_{\text{diffusive}}. \tag{37}$$

This equation relates the SIFS directly to dissipative processes associated with the eddy viscosity and the eddy diffusivity. Thus the SIFS can only occur in the presence of (parameterized) transient eddy PV fluxes (*c.f.* Treguier and McWilliams 1990; Straub 1993). Similarly, we multiply the lower-layer wave equation (Equation (31) with $k = 2$) by $\partial_x \tilde{\psi}_2$ and zonally average to obtain, after further manipulations,

$$\begin{aligned}\mathrm{TFS} = &\underbrace{\frac{r_b}{U_2}\left\langle \left(\partial_x \tilde{\psi}_2\right)^2 \right\rangle_x}_{\text{frictional}} \\ &+ \underbrace{\nu\left[\frac{H_2}{U_2}\left\langle \left(\partial_x^2 \tilde{\psi}_2\right)^2 \right\rangle_x + \frac{H_1}{U_1}\left\langle \left(\partial_x^2 \tilde{\psi}_1\right)^2 \right\rangle_x\right]}_{\text{viscous}} \\ &+ \underbrace{\frac{\kappa f^2}{g'}\left[\frac{1}{U_2}\left\langle \left(\partial_x \tilde{\psi}_2\right)^2 \right\rangle_x + \frac{1}{U_1}\left\langle \left(\partial_x \tilde{\psi}_1\right)^2 \right\rangle_x - \left(\frac{1}{U_2}+\frac{1}{U_1}\right)\left\langle \partial_x \tilde{\psi}_2 \partial_x \tilde{\psi}_1 \right\rangle_x\right]}_{\text{diffusive}}. \end{aligned} \quad (38)$$

This equation relates the TFS directly to dissipative processes associated with the linear friction, the eddy viscosity and the eddy diffusivity. Physically, the relationships (37)–(38) arise because the SIFS and TFS extract energy from the mean flow and convert it to standing wave energy. This standing wave energy source must be balanced by corresponding sinks, which are provided either by frictional energy dissipation or via conversion to transient eddy energy.

In Figure 10 we quantify the contributions of bottom friction, eddy viscosity, and eddy diffusivity to the TFS and SIFS, computed via (37)–(38). In the eddy-saturated regime ($\tau_w^{max} \gtrsim 0.04\,\mathrm{N\,m^{-2}}$), the TFS is primarily (~70%) supported by viscous dissipation, with diffusive and frictional dissipation making relatively minor contributions. Consistent with this, Bai et al. (2021) found that including a horizontal eddy viscosity substantially enhanced the TFS in a similar, barotropic standing wave theory, and was necessary to produce qualitative agreement between the theory and numerical simulations. Physically, this implies that the production of standing wave energy associated with topographic form stress is primarily removed via (parameterized) eddy viscous dissipation. The SIFS is consistently supported in almost equal parts by viscous and diffusive dissipation. Given that (35) holds approximately, and given that the upper-layer zonal velocity is approximately independent of the wind stress (because $U_1 \gg U_2$ and $U_1 - U2$ is insensitive to the wind stress), these diagnostics imply that the rate of standing wave energy dissipation must increase linearly with the wind stress. Noting that the second "diffusive" term in (37) is empirically negligible compared with the first (not shown), this implies that the SKE scales as

$$\mathrm{SKE} \sim \tau_w^{max}. \quad (39)$$

This linear relationship between the standing wave kinetic energy and the wind stress is consistent both with our theoretical solutions in the eddy-saturated regime (Figure 9(d)) and with our channel model simulations (Figure 6(c)).

5. Discussion and Conclusions

This work was motivated by the divergent previous explanations of the "eddy saturation" phenomenon, *i.e.* the approximate independence of the ACC transport to changes in the mean zonal winds. Specifically, various previous studies have either posited that "eddy saturation" occurs as a result of changes in the efficiency of eddy transfer (Marshall and Radko 2003; Meredith et al. 2012; Marshall et al. 2017; Mak et al. 2018), or argued that it occurs as a result of "flexing" of the ACC's standing meanders (Thompson and Naveira Garabato 2014; Nadeau and Ferrari 2015; Constantinou and Hogg 2019). As is evident from the alongstream-averaged momentum balance utilized in this study, eddies play a central role in the downward transfer of wind-input momentum (see Figures 1 and 3), or equivalently the southward transport of heat (Vallis 2006). This is consistent with previous studies showing that eddy heat fluxes across mean streamlines are approximately equal to the combined heat flux due to standing plus transient eddies across lines of constant latitude (Marshall et al. 1993; Abernathey and Cessi 2014). The focus of this study is on the mechanisms via which this downward transfer of momentum along mean streamlines by transient eddies responds to changes in the surface wind stress. As shown in Section 2b, changes in this transient eddy momentum transfer results from a combination of: a) changes in the efficiency with which the eddy field transfers momentum down the vertical gradient in the mean flow; or b) a restructuring of the mean flow that allows the eddies to transfer more momentum downward in a circumpolar integral. The former corresponds to an increase in the eddy diffusivity, κ, as discussed in Section 2c. The latter may correspond to a combination of lengthening of the standing meanders (Thompson and Naveira Garabato 2014) and spin-up of gyres abutting the circumpolar flow (Nadeau and Ferrari 2015), which we collectively refer to as an adjustment of the "standing waves".

In this study we sought to distinguish between these previously-proposed mechanisms of "eddy saturation" via analysis of hundreds of simulations using an eddy-resolving, two-layer channel model (Section 2a). These simulations exhibit saturation of the zonal transport (Figure 5), with changes in wind-input momentum being accommodated by changes in the eddy IFS along mean streamlines (Figure 7). To isolate the mechanism of "eddy

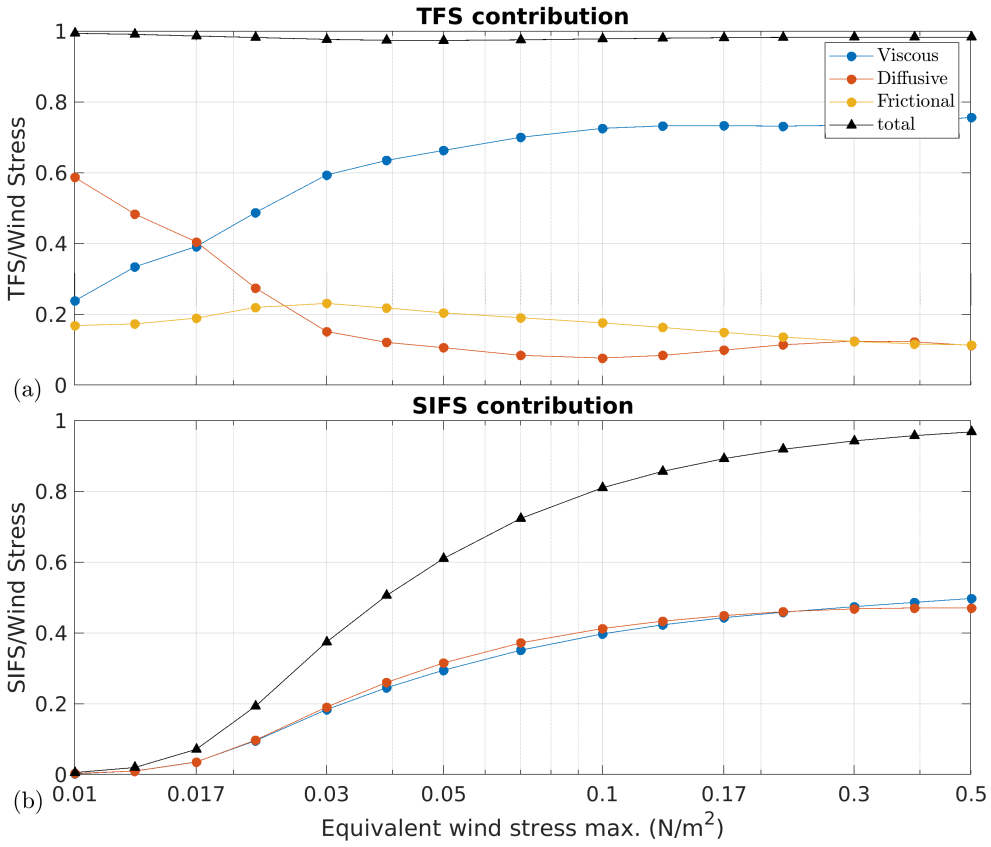

FIG. 10. Black curves show the magnitudes of (a) topographic form stress (TFS) and (b) standing wave interfacial form stress (SIFS) to the zonal momentum balance in our quasi-geostrophic theory, normalized by the zonal wind stress (Equations (32a)–(32b)). Colored curves show the decomposition of the TFS into contributions from viscous, diffusive and frictional energy dissipation (Equations (37)–(38)). We hold the linear friction velocity constant and equal to $r_b = 4\times10^{-4}\,\mathrm{m\,s^{-1}}$ for clarity. The "equivalent wind stress maximum" defines the wind stress profile via (5), which is then meridionally averaged and used to force the theoretical momentum equation (32a).

saturation", we therefore decomposed the alongstream-averaged eddy IFS into multiplicative contributions from the eddy diffusivity and the structure of the mean flow (Equation (17)). We then separately diagnosed κ and the mean flow from each of our model simulations, allowing us to create approximate reconstructions of the alongstream-averaged eddy IFS (Figure 3). Via reconstructions based on independent variations of κ and the mean flow, we showed that varying the mean flow alone approximately reconstructs the diagnosed eddy IFS across our suite of experiments (Figure 7). In contrast, varying κ alone yields a much less accurate reconstruction of the diagnosed eddy IFS; indeed, for a realistic range of wind stresses ($\gtrsim 0.1\,\mathrm{N\,m^{-2}}$) the eddy IFS is approximately insensitive to variations in κ. We therefore concluded that, at least in this suite of model simulations, "eddy saturation" is primarily attributable to adjustment of standing waves, rather than transient eddies.

Motivated by this finding, we posed a quasi-geostrophic theory of our idealized ACC in which κ is held constant, and thus saturation can only occur via adjustment of standing waves (Section 4a). This theory is distinguished from previous studies (*e.g.* Abernathey and Cessi 2014) primarily via the separate treatment of eddy vertical momentum transfer, proportional to κ, and lateral eddy momentum fluxes, proportional to the eddy viscosity ν. However, the assumptions underpinning the theory produce qualitative differences from our channel model simulations (compare Figures 3(a) and 8). Thus, while the theory serves to demonstrate that eddy saturation can occur purely via adjustment of standing waves (Figure 9), it is difficult to directly compare its predictions with the diagnostics from our simulations. Furthermore, one might hope that the relative simplicity of our theory might facilitate the derivation of further simplified scalings, for example to elucidate the parameter dependence of the zonal transport. Though our

efforts have failed to acquire such insights thus far, further study of the model equations may prove fruitful. The theory nonetheless offers transferable insights into the dynamics of standing wave-induced saturation; for example, it predicts that the standing wave kinetic energy must increase linearly with the wind stress in order to produce a saturated zonal transport (Figures 6(c) and 9(d) and Section 4c).

A caveat of our overall approach is that the posing of our channel model simulations and quasi-geostrophic theory is highly idealized, which raises questions regarding the transferability of our findings to more realistic model configurations and to nature. Future studies could test our conclusions by extending the eddy IFS decomposition (Section 2b) and mean flow eddy diffusivity perturbation analysis (Section 3) to more realistic model configurations. A specific caveat of this perturbation analysis is that it simplistically perturbs the mean flow or κ at each horizontal point in space (see Figure 7), which could skew the resulting eddy IFS calculations in some situations. For example, if we applied a wind perturbation of sufficient magnitude to substantially shift the path of the mean flow over the topographic ridge, then the mean flow streamlines in that simulation may no longer traverse the region of maximum EKE and κ in the reference simulation (Figure 4), and this may be expected to bias the calculation toward a smaller eddy IFS. This may explain why the reconstructed eddy IFS with fixed κ and varying mean flow under-predicts the diagnosed eddy IFS in the experiments with the largest wind stresses (Figure 7(b–c)). It may be possible to circumvent such issues via more dynamically-based perturbations; for example, one might be able to empirically derive a relationship between κ and the mean flow ($\overline{\boldsymbol{u}}$) in each experiment, *i.e.* $\kappa \approx \kappa(\overline{\boldsymbol{u}})$, and then attempt to reconstruct the eddy IFS by independently perturbing $\overline{\boldsymbol{u}}$ and the functional relationship $\kappa(\overline{\boldsymbol{u}})$ across all of the experiments.

It also remains to be understood why this and previous model studies have exhibited apparently contradictory mechanisms of eddy saturation. For example, previous modeling studies that have argued for saturation by transient eddy adjustment (Meredith et al. 2012; Munday et al. 2013; Marshall et al. 2017; Mak et al. 2018) have reported that the EKE scales linearly with the wind stress, whereas in our simulations it scales sub-linearly (Figure 6). A common feature of these previous studies is that they use a linear formulation of the bottom friction; this, in part, motivated us to conduct a parallel suite of experiments with linear bottom friction (see Appendix B). For weak winds stresses ($\lesssim 0.1\,\mathrm{N\,m^{-2}}$), independently varying κ more accurately reproduces the changes in the diagnosed alongstream eddy IFS than does independently varying the mean flow, indicating that the saturation may be a result of transient eddy adjustments. However, for a realistic range of wind stresses ($\gtrsim 0.1\,\mathrm{N\,m^{-2}}$) the transport saturation appears to be better explained by variations in the mean flow. These experiments suggest that the formulation of bottom friction may be an essential element of "eddy saturation". Further work is required to assess whether this does indeed explain the differences in saturation behavior proposed in previous modeling studies, and perhaps to assess which formulation of bottom friction is most accurate at the scales of motion represented by the models (Arbic and Scott 2008).

In addition to partly reconciling previous explanations of the "eddy saturation" phenomenon, these findings also have implications for coarsely-resolved ocean/climate model simulations that must parameterize the effects of mesoscale eddies (Gent and McWilliams 1990; Gent et al. 1995). If "eddy saturation" is primarily the result of transient eddy adjustments, then this motivates the use of parameterization schemes that allow κ to adapt to changes in surface wind stress (Marshall and Radko 2003; Mak et al. 2018, 2022). In contrast, if saturation is primarily the result of standing wave adjustments then much simpler parameterization schemes may suffice, provided that the standing waves are resolved. Consistent with the latter, (Farneti et al. 2015) found that an ensemble of interannually-forced, coarse-resolution global ocean simulations consistently exhibited independence of the baroclinic transport from the wind stress. Kong and Jansen (2021) compared simulations with resolved and parameterized eddies in an idealized Southern Ocean sector model. They found that even a coarse simulation with a constant κ had a similar wind forcing response to that of an eddy-resolving simulation, consistent with our idealized quasi-geostrophic theory. These findings suggest that the key to representing "eddy saturation" in coarse ocean/climate models is to resolve or parameterize the standing wave response, rather than the transient eddy response, to wind changes.

Acknowledgments. This material is based in part upon work supported by the National Science Foundation under Grant Numbers OCE-1751386 and OPP-2023244, and by the National Aeronautics and Space Administration ROSES Physical Oceanography program under grant number 80NSSC19K1192. This work used the Extreme Science and Engineering Discovery Environment (XSEDE, Towns et al. 2014), which is supported by National Science Foundation grant number ACI-1548562. The authors thank two anonymous reviewers for comments that improved the submitted manuscript, and editor Paola Cessi for handling the peer-review process.

Data availability statement. The AWSIM model code used in this study can be obtained from `https://github.com/andystew7583/AWSIM`. The codes used to configure and analyze our model simulations are available via `https://doi.org/10.5281/zenodo.6850435`.

APPENDIX A

Momentum balance in latitudinal and streamline coordinates

In this Appendix we provide complete expressions for the isopycnal momentum balances discussed in Section 2b and presented in Figure 3. In all of these expressions the hyperviscous stress tensor and the diapycnal (restoring) velocity, all of which contribute negligibly to the zonally- or alongstream-averaged momentum balance. We neglect the Coriolis term because there is no overturning circulation in our model simulations, and thus this term is also negligible.

a. Zonally-averaged momentum balance

The depth-integrated, zonally-averaged zonal momentum balance is given by

$$\underbrace{\frac{\partial}{\partial t}\sum_k \left\langle \overline{h_k}\widehat{u_k}\right\rangle_x}_{\text{tendency}} \approx \underbrace{-\sum_k \frac{\partial}{\partial y}\left\langle \overline{h_k}\widehat{v_k}\widehat{u_k}\right\rangle_x}_{\text{mean advection}} \underbrace{-\sum_k \frac{\partial}{\partial y}\left\langle \overline{h_k}\widehat{v_k^\dagger u_k^\dagger}\right\rangle_x}_{\text{eddy advection}} \underbrace{-\sum_k \left\langle \overline{h_k}\partial_x \overline{M_k}\right\rangle_x}_{\text{topographic form stress}} + \underbrace{\frac{\tau_w}{\rho_0}}_{\text{wind stress}} \underbrace{-\frac{1}{\rho_0}\left\langle \overline{\tau_b^{(x)}}^t\right\rangle_x}_{\text{bottom friction}}, \quad \text{(A1)}$$

and the upper layer zonally-averaged zonal momentum balance is given by

$$\underbrace{\frac{\partial}{\partial t}\left\langle \overline{h_1}\widehat{u_1}\right\rangle_x}_{\text{tendency}} \approx \underbrace{-\frac{\partial}{\partial y}\left\langle \overline{h_1}\widehat{v}_1\widehat{u}_1\right\rangle_x}_{\text{mean advection}} \underbrace{-\frac{\partial}{\partial y}\left\langle \overline{h_1}\widehat{v_1^\dagger u_1^\dagger}\right\rangle_x}_{\text{eddy advection}} \underbrace{-\left\langle \overline{h_1}\partial_x \overline{M_1}\right\rangle_x}_{\text{mean IFS}} \underbrace{-\left\langle h_1'\partial_x M_1'\right\rangle_x}_{\text{eddy IFS}} + \underbrace{\frac{\tau_w}{\rho_0}}_{\text{wind stress}}. \quad \text{(A2)}$$

b. Alongstream-averaged momentum balance

To present the alongstream-averaged momentum balance, we first define the alongstream-averaging operator for an arbitrary vector $\boldsymbol{a}$,

$$\langle \boldsymbol{a}\rangle_M = \frac{1}{L_x}\oint_{\overline{\zeta}=\zeta_0} \boldsymbol{a}\cdot \mathrm{d}\boldsymbol{s}. \quad \text{(A3)}$$

The depth-integrated, alongstream-averaged momentum balance is then

$$\underbrace{\frac{\partial}{\partial t}\sum_k \left\langle \overline{h_k}\widehat{\boldsymbol{u}_k}\right\rangle_M}_{\text{tendency}} \approx \underbrace{-\sum_k \left\langle \nabla\cdot\left(\overline{h_k}\widehat{\boldsymbol{u}}_k\widehat{\boldsymbol{u}}_k\right)\right\rangle_M}_{\text{mean advection}} \underbrace{-\sum_k \left\langle \nabla\cdot\left(\overline{h_k}\widehat{\boldsymbol{u}_k^\dagger \boldsymbol{u}_k^\dagger}\right)\right\rangle_M}_{\text{eddy advection}} \underbrace{-\left\langle \overline{h_k}\nabla\overline{M_k}\right\rangle_M}_{\text{topographic form stress}} + \underbrace{\left\langle \frac{\tau_w}{\rho_0}\hat{\boldsymbol{x}}\right\rangle_M}_{\text{wind stress}} \underbrace{-\left\langle \frac{\boldsymbol{\tau}_b}{\rho_0}\right\rangle_M}_{\text{bottom friction}}, \quad \text{(A4)}$$

and the upper layer alongstream-averaged momentum balance is

$$\underbrace{\frac{\partial}{\partial t}\left\langle \overline{h_1}\widehat{\boldsymbol{u}_1}\right\rangle_M}_{\text{tendency}} \approx \underbrace{-\left\langle \nabla\cdot\left(\overline{h_1}\widehat{\boldsymbol{u}_1}\widehat{\boldsymbol{u}_1}\right)\right\rangle_M}_{\text{mean advection}} \underbrace{-\left\langle \nabla\cdot\left(\overline{h_1}\widehat{\boldsymbol{u}_1^\dagger \boldsymbol{u}_1^\dagger}\right)\right\rangle_M}_{\text{eddy advection}} \underbrace{-\left\langle \overline{h_1'\nabla M_1'}\right\rangle_M}_{\text{eddy IFS}} + \underbrace{\left\langle \frac{\tau_w}{\rho_0}\hat{\boldsymbol{x}}\right\rangle_M}_{\text{wind stress}}. \quad \text{(A5)}$$

APPENDIX B

Simulations with linear bottom friction

In this Appendix we reproduce the results presented in Section 3 using diagnostics from our suite of experiments with a linear, rather than quadratic, formulation of the bottom friction.

Figure B1 shows the sensitivity of the total, barotropic and baroclinic transports to variations in the wind stress and linear friction velocity. These sensitivities closely resemble those shown in Figure 5, albeit with a somewhat larger range of transports in response to the range of friction velocities explored here.

Figure B2 shows the sensitivity of the transient eddy diffusivity (averaged over the "storm track" region), the domain-averaged eddy kinetic energy, and the domain-averaged standing wave kinetic energy to variations in the wind stress and linear friction velocity. These sensitivities also qualitatively resemble their counterparts in Figure 6. However, in these simulations κ and EKE increase with wind stress slightly faster than in the simulations with quadratic friction: least-squares fits over all of our simulations yield $\kappa \sim \tau^{0.7}$ and EKE $\sim \tau^{0.8}$.

Figure B3 shows our reconstruction of the eddy IFS resulting from independent variations of the eddy diffusivity and the mean flow across our suite of simulations.

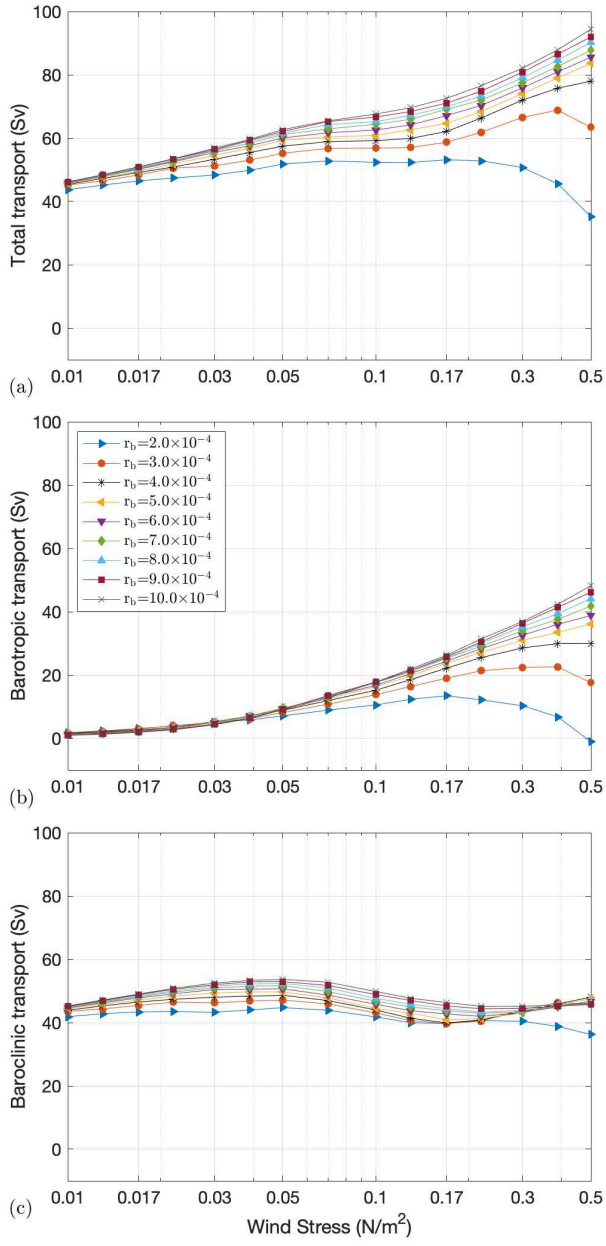

FIG. B1. As Figure 5, but with diagnostics drawn from our suite of channel model simulations with a linear formulation of the bottom friction.

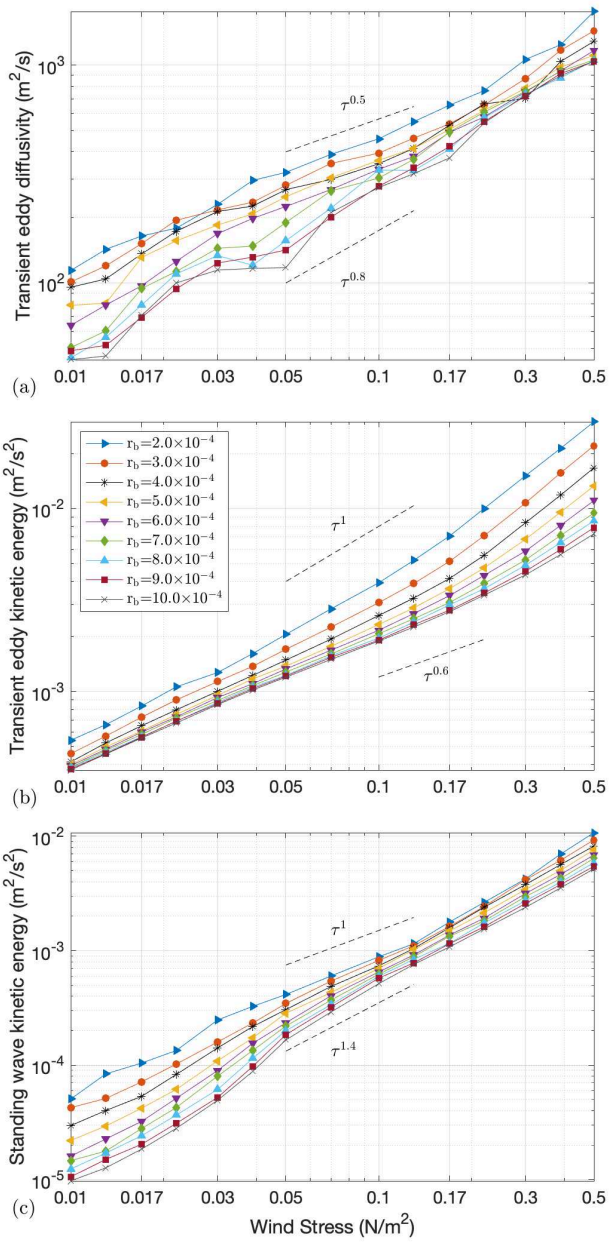

FIG. B2. As Figure 6, but with diagnostics drawn from our suite of channel model simulations with a linear formulation of the bottom friction.

Similar to our simulations with quadratic bottom friction, the eddy IFS consistently dominates the alongstream momentum balance. However, the results of our eddy IFS reconstructions differ substantially from our experiments with quadratic bottom friction, with distinct behaviors for wind stresses larger than the reference case versus smaller than the reference case. For larger wind stresses, holding κ fixed and varying the mean flow provides a more accurate reconstruction of the eddy IFS, although the accuracy is lower than found in the quadratic friction experiments (see Figure 7). For smaller wind stresses, the result is reversed: holding the mean flow fixed and varying κ provides a more accurate reconstruction of the eddy IFS. In contrast, holding κ fixed and varying the mean flow leads to the eddy IFS decreasing too rapidly with the wind stress.

APPENDIX C

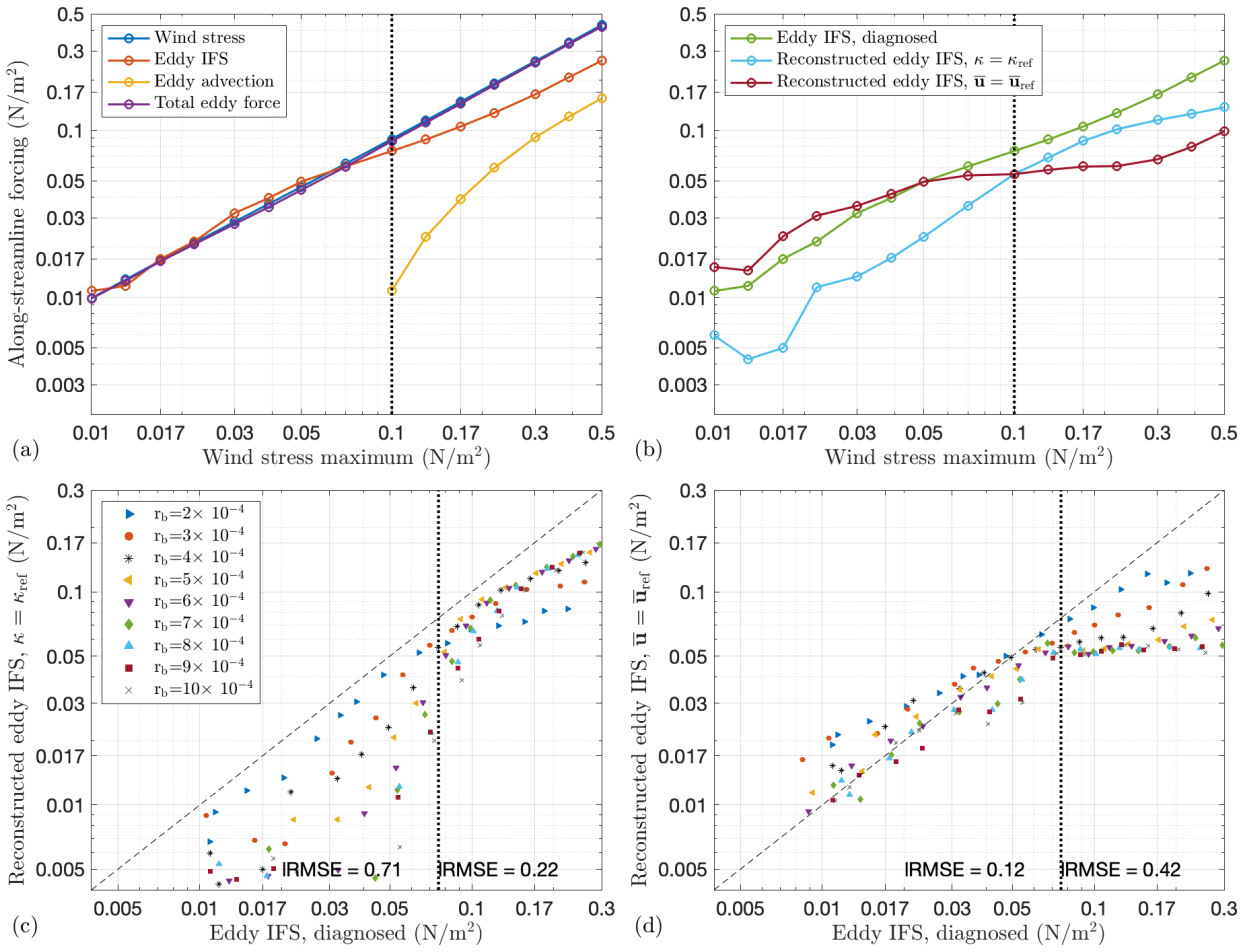

FIG. B3. As Figure 7, but with diagnostics drawn from our suite of channel model simulations with a linear formulation of the bottom friction. In this figure we have added dotted lines to indicate our reference experiment.

Eddy interfacial form stress along latitude lines

Our quasi-geostrophic theory of "eddy saturation" (see Section 4) employs a different eddy diffusivity $\kappa^{(y)}$ to parameterize transient eddy transfer of momentum down the vertical gradient of the zonal-mean flow. Here we justify this choice via analysis of the zonally-integrated zonal momentum balance. Figure C1(a) shows the domain-averaged zonal wind stress, zonal component of the mean IFS and zonal component of the eddy IFS for experiments with varying wind stress maxima and constant quadratic drag coefficient $C_\mathrm{d} = 2\times10^{-3}$. Consistent with Figure 3, the downward transfer of momentum is consistently dominated by the mean IFS, with the eddy IFS reaching at most 20% of the wind stress for very weak wind stresses. We estimate $\kappa^{(y)}$ using the domain-averaged zonal component of the eddy IFS and the domain-averaged zonal mean flow via

$$\kappa^{(y)} = \frac{g'}{\rho_0 f^2}\frac{\int_0^{L_y}\mathrm{d}y\left\langle\overline{p'_\eta\partial_x\eta'}\right\rangle_x}{\int_0^{L_y}\mathrm{d}y\,\langle\widehat{u_1}-\widehat{u_2}\rangle_x}. \tag{C1}$$

Figure C1 shows that the diagnosed $\kappa^{(y)}$ across our suite of experiments with varying wind stresses and quadratic drag coefficients. For wind stress maxima smaller than $\sim0.17\,\mathrm{N\,m^{-2}}$, $\kappa^{(y)}$ typically lies between 0 and $100\,\mathrm{m^2\,s^{-1}}$, depending on the drag coefficient. For larger wind stress maxima the diagnosed $\kappa^{(y)}$ varies widely with the drag coefficient, with various experiments seemingly simulating up-gradient momentum transfer by transient eddies in a domain-average.

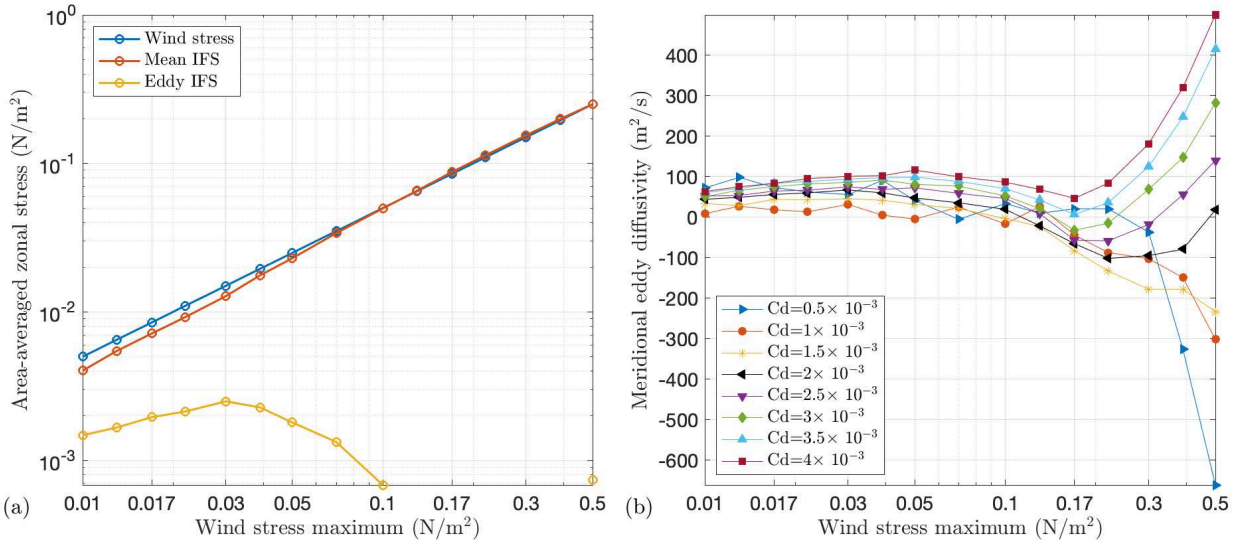

FIG. C1. Diagnostics of the zonally-integrated eddy interfacial form stress (IFS) in our simulations with quadratic bottom friction. (a) Domain-integrated zonal wind stress, zonal component of the mean IFS, and zonal component of the eddy IFS in simulations with varying wind stress and fixed quadratic drag coefficient $C_d = 2 \times 10^{-3}$. (b) Meridional eddy diffusivity (see Appendix C) as a function of the wind stress and the quadratic drag coefficient.

References

Abernathey, R., and P. Cessi, 2014: Topographic enhancement of eddy efficiency in baroclinic equilibration. *J. Phys. Oceanogr.*, **44 (8)**, 2107–2126.

Aiki, H., X. Zhai, and R. J. Greatbatch, 2016: Energetics of the global ocean: The role of mesoscale eddies. *Indo-Pacific climate variability and predictability*, 109–134.

Arbic, B. K., and R. B. Scott, 2008: On quadratic bottom drag, geostrophic turbulence, and oceanic mesoscale eddies. *J. Phys. Oceanogr.*, **38 (1)**, 84–103.

Bai, Y., Y. Wang, and A. L. Stewart, 2021: Does Topographic Form Stress Impede Prograde Ocean Currents? *J. Phys. Oceanogr.*, **51**, 2617–2638, URL https://doi.org/10.1175/JPO-D-20-0189.1.

Bischoff, T., and A. F. Thompson, 2014: Configuration of a Southern Ocean storm track. *J. Phys. Oceanogr.*, **44 (12)**, 3072–3078.

Böning, C. W., A. Dispert, M. Visbeck, S. R. Rintoul, and F. U. Schwarzkopf, 2008: The response of the Antarctic Circumpolar Current to recent climate change. *Nature Geosci.*, **1 (12)**, 864–869.

Chelton, D. B., R. A. De Szoeke, M. G. Schlax, K. El Naggar, and N. Siwertz, 1998: Geographical variability of the first baroclinic Rossby radius of deformation. *J. Phys. Oceanogr.*, **28 (3)**, 433–460.

Constantinou, N. C., and A. M. Hogg, 2019: Eddy saturation of the Southern Ocean: A baroclinic versus barotropic perspective. *Geophys. Res. Lett.*, **46 (21)**, 12 202–12 212.

Constantinou, N. C., and W. R. Young, 2018: Beta-plane turbulence above monoscale topography. *J. Fluid Mech.*, **827**, 415–447.

Davey, M. K., 1980: A quasi-linear theory for rotating flow over topography. Part 1. Steady β-plane channel. *J. Fluid Mech.*, **99 (2)**, 267–292.

Donohue, K. A., K. L. Tracey, D. R. Watts, M. P. Chidichimo, and T. K. Chereskin, 2016: Mean Antarctic Circumpolar Current transport measured in Drake Passage. *Geophys. Res. Lett.*, **43 (22)**, 11–760.

Farneti, R., and Coauthors, 2015: An assessment of Antarctic Circumpolar Current and Southern Ocean meridional overturning circulation during 1958–2007 in a suite of interannual CORE-II simulations. *Ocean Modell.*, **93**, 84–120.

Ferrari, R., and M. Nikurashin, 2010: Suppression of eddy diffusivity across jets in the Southern Ocean. *J. Phys. Oceanogr.*, **40 (7)**, 1501–1519.

Gent, P. R., and J. C. McWilliams, 1990: Isopycnal mixing in ocean circulation models. *J. Phys. Oceanogr.*, **20 (1)**, 150–155.

Gent, P. R., J. Willebrand, T. J. McDougall, and J. C. McWilliams, 1995: Parameterizing eddy-induced tracer transports in ocean circulation models. *J. Phys. Oceanogr.*, **25 (4)**, 463–474.

Gill, A. E., 1982: *Atmosphere-ocean dynamics*, Vol. 30. Academic press.

Greatbatch, R. J., and K. G. Lamb, 1990: On parameterizing vertical mixing of momentum in non-eddy resolving ocean models. *J. Phys. Oceanogr.*, **20 (10)**, 1634–1637.

Griffies, S. M., and R. W. Hallberg, 2000: Biharmonic friction with a Smagorinsky-like viscosity for use in large-scale eddy-permitting ocean models. *Mon. Weather Rev.*, **128 (8)**, 2935–2946.

Hallberg, R., 2013: Using a resolution function to regulate parameterizations of oceanic mesoscale eddy effects. *Ocean Modell.*, **72**, 92–103.

Hazel, J. E., and A. L. Stewart, 2019: Are the near-Antarctic easterly winds weakening in response to enhancement of the southern annular mode? *J. Climate*, **32 (6)**, 1895–1918.

Hogg, A. M., and J. R. Blundell, 2006: Interdecadal variability of the Southern Ocean. *J. Phys. Oceanogr.*, **36 (8)**, 1626–1645.

Hogg, A. M. C., M. P. Meredith, J. R. Blundell, and C. Wilson, 2008: Eddy heat flux in the Southern Ocean: response to variable wind forcing. *J. Climate*, **21 (4)**, 608–620.

Howard, E., A. M. Hogg, S. Waterman, and D. P. Marshall, 2015: The injection of zonal momentum by buoyancy forcing in a Southern Ocean model. *J. Phys. Oceanogr.*, **45 (1)**, 259–271.

Johnson, G. C., and H. L. Bryden, 1989: On the size of the Antarctic Circumpolar Current. *Deep Sea Res. Pt. A*, **36 (1)**, 39–53.

Kong, H., and M. F. Jansen, 2021: The impact of topography and eddy parameterization on the simulated Southern Ocean circulation response to changes in surface wind stress. *J. Phys. Oceanogr.*, **51 (3)**, 825–843.

Large, W. G., and S. G. Yeager, 2009: The global climatology of an interannually varying air–sea flux data set. *Climate Dynam.*, **33 (2)**, 341–364.

LeVeque, R. J., 2002: *Finite volume methods for hyperbolic problems*, Vol. 31. Cambridge university press.

Maddison, J. R., and D. P. Marshall, 2013: The Eliassen–Palm flux tensor. *J. Fluid Mech.*, **729**, 69–102.

Mak, J., J. R. Maddison, D. P. Marshall, and D. R. Munday, 2018: Implementation of a geometrically informed and energetically constrained mesoscale eddy parameterization in an ocean circulation model. *J. Phys. Oceanogr.*, **48 (10)**, 2363–2382.

Mak, J., D. P. Marshall, G. Madec, and J. R. Maddison, 2022: Acute sensitivity of global ocean circulation and heat content to eddy energy dissipation timescale. *Geophys. Res. Lett.*, **49 (8)**, e2021GL097 259.

Marshall, D. P., 2016: A theoretical model of long Rossby waves in the Southern Ocean and their interaction with bottom topography. *Fluids*, **1 (2)**, 17.

Marshall, D. P., M. H. P. Ambaum, J. R. Maddison, D. R. Munday, and L. Novak, 2017: Eddy saturation and frictional control of the Antarctic Circumpolar Current. *Geophys. Res. Lett.*, **44 (1)**, 286–292.

Marshall, D. P., J. R. Maddison, and P. S. Berloff, 2012: A framework for parameterizing eddy potential vorticity fluxes. *J. Phys. Oceanogr.*, **42 (4)**, 539–557.

Marshall, J., D. Olbers, H. Ross, and D. Wolf-Gladrow, 1993: Potential vorticity constraints on the dynamics and hydrography of the Southern Ocean. *J. Phys. Oceanogr.*, **23 (3)**, 465–487.

Marshall, J., and T. Radko, 2003: Residual-mean solutions for the Antarctic Circumpolar Current and its associated overturning circulation. *J. Phys. Oceanogr.*, **33 (11)**, 2341–2354.

Marshall, J., and T. Radko, 2006: A model of the upper branch of the meridional overturning of the southern ocean. *Prog. Oceanogr.*, **70 (2-4)**, 331–345.

Marshall, J., and G. Shutts, 1981: A note on rotational and divergent eddy fluxes. *J. Phys. Oceanogr.*, **11 (12)**, 1677–1680.

Marshall, J., and K. Speer, 2012: Closure of the meridional overturning circulation through Southern Ocean upwelling. *Nature Geosci.*, **5 (3)**, 171–180.

Mayewski, P. A., and Coauthors, 2009: State of the Antarctic and Southern Ocean climate system. *Rev. Geophys.*, **47 (1)**.

Meredith, M. P., 2016: Understanding the structure of changes in the Southern Ocean eddy field. *Geophys. Res. Lett.*, **43 (11)**, 5829–5832.

Meredith, M. P., and A. M. Hogg, 2006: Circumpolar response of Southern Ocean eddy activity to a change in the Southern Annular Mode. *Geophys. Res. Lett.*, **33 (16)**.

Meredith, M. P., A. C. Naveira Garabato, A. M. Hogg, and R. Farneti, 2012: Sensitivity of the overturning circulation in the Southern Ocean to decadal changes in wind forcing. *J. Climate*, **25 (1)**, 99–110.

Munday, D. R., H. L. Johnson, and D. P. Marshall, 2013: Eddy saturation of equilibrated circumpolar currents. *J. Phys. Oceanogr.*, **43 (3)**, 507–532.

Munk, W. H., and E. Palmén, 1951: Note on the dynamics of the Antarctic Circumpolar Current. *Tellus*, **3 (1)**, 53–55.

Nadeau, L.-P., and R. Ferrari, 2015: The role of closed gyres in setting the zonal transport of the antarctic circumpolar current. *Journal of Physical Oceanography*, **45 (6)**, 1491 – 1509, https://doi.org/10.1175/JPO-D-14-0173.1, URL https://journals.ametsoc.org/view/journals/phoc/45/6/jpo-d-14-0173.1.xml.

Nowlin Jr, W. D., and J. M. Klinck, 1986: The physics of the Antarctic circumpolar current. *Rev. Geophys.*, **24 (3)**, 469–491.

Olbers, D., D. Borowski, C. Völker, and J.-O. Woelff, 2004: The dynamical balance, transport and circulation of the Antarctic Circumpolar Current. *Antarct. Sci.*, **16 (4)**, 439–470.

Pedlosky, J., 1987: *Geophysical fluid dynamics*. Springer.

Rintoul, S. R., 2018: The global influence of localized dynamics in the Southern Ocean. *Nature*, **558 (7709)**, 209–218.

Stewart, A. L., and P. J. Dellar, 2016: An energy and potential enstrophy conserving numerical scheme for the multi-layer shallow water equations with complete Coriolis force. *J. Comput. Phys.*, **313**, 99–120.

Stewart, A. L., and A. M. Hogg, 2017: Reshaping the Antarctic Circumpolar Current via Antarctic Bottom Water Export. *J. Phys. Oceanogr.*, **47 (10)**, 2577–2601.

Stewart, A. L., J. C. McWilliams, and A. Solodoch, 2021: On the role of bottom pressure torques in wind-driven gyres. *J. Phys. Oceanogr.*, **51 (5)**, 1441–1464.

Straub, D. N., 1993: On the transport and angular momentum balance of channel models of the Antarctic Circumpolar Current. *J. Phys. Oceanogr.*, **23 (4)**, 776–782.

Talley, L. D., 2013: Closure of the global overturning circulation through the Indian, Pacific, and Southern Oceans: Schematics and transports. *Oceanography*, **26 (1)**, 80–97.

Thompson, A. F., and A. C. Naveira Garabato, 2014: Equilibration of the Antarctic Circumpolar Current by standing meanders. *J. Phys. Oceanogr.*, **44 (7)**, 1811–1828.

Thompson, D. W. J., and S. Solomon, 2002: Interpretation of recent Southern Hemisphere climate change. *Science*, **296 (5569)**, 895–899.

Toggweiler, J. R., 2009: Shifting westerlies. *Science*, **323 (5920)**, 1434–1435.

Toggweiler, J. R., J. . Russell, and S. R. Carson, 2006: Midlatitude westerlies, atmospheric CO2, and climate change during the ice ages. *Paleoceanography*, **21 (2)**.

Towns, J., and Coauthors, 2014: XSEDE: Accelerating scientific discovery. *Computing in Science & Engineering*, **16 (5)**, 62–74, https://doi.org/10.1109/MCSE.2014.80.

Treguier, A.-M., and J. McWilliams, 1990: Topographic influences on wind-driven, stratified flow in a β-plane channel: An idealized model for the antarctic circumpolar current. *Journal of Physical Oceanography*, **20**, 321–343, https://doi.org/10.1175/1520-0485(1990)020<0321:TIOWDS>2.0.CO;2.

Vallis, G. K., 2006: *Atmospheric and oceanic fluid dynamics: fundamentals and large-scale circulation*. Cambridge Univ Pr.

Ward, M. L., and A. M. Hogg, 2011: Establishment of momentum balance by form stress in a wind-driven channel. *Ocean Modell.*, **40 (2)**, 133–146.

Whitworth, T., and R. G. Peterson, 1985: Volume Transport of the Antarctic Circumpolar Current from Bottom Pressure Measurements. *J. Phys. Oceanogr.*, **15 (6)**, 810–816.

Young, W. R., 2012: An exact thickness-weighted average formulation of the boussinesq equations. *J. Phys. Oceanogr.*, **42 (5)**, 692–707.

Youngs, M. K., G. R. Flierl, and R. Ferrari, 2019: Role of residual overturning for the sensitivity of southern ocean isopycnal slopes to changes in wind forcing. *Journal of Physical Oceanography*, **49 (11)**, 2867 – 2881, https://doi.org/10.1175/JPO-D-19-0072.1, URL https://journals.ametsoc.org/view/journals/phoc/49/11/jpo-d-19-0072.1.xml.

Youngs, M. K., A. F. Thompson, A. Lazar, and K. J. Richards, 2017: Acc meanders, energy transfer, and mixed barotropic–baroclinic instability. *J. Phys. Oceanogr.*, **47 (6)**, 1291–1305.